STRUCTURAL BIOLOGY

Structural architecture of TolQ-TolR inner membrane protein complex from opportunistic pathogen *Acinetobacter baumannii*

Elina Karimullina[1,2], Yirui Guo[3,4], Hanif M. Khan[5], Tabitha Emde[2,3], Bradley Quade[3], Rosa Di Leo[2,6], Zbyszek Otwinowski[2,3,7], D. Peter Tieleman[5], Dominika Borek[2,3,7], Alexei Savchenko[1,2]*

Gram-negative bacteria harness the proton motive force (PMF) within their inner membrane (IM) to uphold cell envelope integrity, an indispensable aspect for both division and survival. The IM TolQ-TolR complex is the essential part of the Tol-Pal system, serving as a conduit for PMF energy transfer to the outer membrane. Here we present cryo–electron microscopy reconstructions of *Acinetobacter baumannii* TolQ in apo and TolR-bound forms at atomic resolution. The apo TolQ configuration manifests as a symmetric pentameric pore, featuring a transmembrane funnel leading toward a cytoplasmic chamber. In contrast, the TolQ-TolR complex assumes a proton nonpermeable stance, characterized by the TolQ pentamer's flexure to accommodate the TolR dimer, where two protomers undergo a translation-based relationship. Our structure-guided analysis and simulations support the rotor-stator mechanism of action, wherein the rotation of the TolQ pentamer harmonizes with the TolR protomers' interplay. These findings broaden our mechanistic comprehension of molecular stator units empowering critical functions within the Gram-negative bacterial cell envelope.

INTRODUCTION

The cell envelope is a complex barrier system that shields bacterial cytoplasm and facilitates bacterial survival in a rapidly changing environment. In Gram-negative bacteria, the canonical structure of the cell envelope consists of a peptidoglycan (PG) layer sandwiched between outer and inner bilayer lipid-based membranes. The outer membrane (OM) composition is asymmetric with the inner phospholipid layer and the outer layer made of lipopolysaccharide. Lacking systems to power active processes in OM, Gram-negative bacteria have evolved protein complexes spanning the cell envelope and connecting OM with the inner membrane (IM). Such systems allow for the energy generated by the proton motive force (PMF) in the IM to be used to drive reactions at OM. One such system is called Tol-Pal, in which the energy-transducing IM complex composed of TolQ, TolR, and TolA proteins, using PMF energy to modulate interactions of TolA with components of the TolB-Pal OM complex (*1*–*5*) (Fig. 1A). The Tol-Pal system is involved in the remodeling of PG at cell division sites and is implicated in other cell division steps involving OM invagination (*6*–*8*). Indispensable for Gram-negative cell envelope Tol-Pal protein complex is targeted by bacterial toxins—colicins—and is a frequent entry point for filamentous phages (*9*, *10*), which exploit pulling-in mechanical force generation by TolQ-TolR-TolA complex.

Previous studies of Tol-Pal complex components have established some characteristics of individual components of this system. For TolA protein, three domains with distinct functions were identified. The N-terminal domain of TolA is embedded into IM and is followed by the long linker domain and C-terminal domains; both the linker domain and the C-terminal domains are shown to be responsible for interactions with various components of OM or proteins associated with OM (*1*), including TolB (*11*). TolR is a small protein that is predicted to contain a single N-terminal α-helical transmembrane domain (TMD) followed by a periplasmic domain that is expected to undergo a structural transition to make contacts with the PG layer (*12*, *13*). The TolQ has been described as a multipass transmembrane protein containing three TMDs and a large cytoplasmic insertion domain located between the first and second TMDs (Fig. 1A) (*13*–*16*). Mutations in IM segments of all three proteins result in severe phenotypic aberrations, which emphasize the importance of interactions in TolQ-TolR-TolA complex (*1*, *3*, *17*–*21*). In *Escherichia coli*, the point mutations in TolQ transmembrane segments alter the cell envelope integrity (*14*) and result in ribonuclease I leakage and formation of OM vesicles (*1*). Similarly, point mutations in TolQ affected the permeability of the cell envelope in *Salmonella typhimurium* (*22*) and bacteremia-causing *Erwinia chrysanthemi* (*23*, *24*), sensitizing these bacteria to bile salts and decreasing their survival. While Δ*tolQ* is not lethal in *E. coli*, it causes reduced O7 lipopolysaccharide expression, lower motility, and deficiency in colonization (*25*, *26*). Δ*tolQ* mutants of *Edwardsiella ictalurid* (*27*), *S. typhimurium* (*22*), and *S. holeraesuis* (*28*) also demonstrated decreased virulence.

The established role of the Tol-Pal system in the virulence and survival of Gram-negative bacteria during pathogenesis makes it an attractive target for antibacterial intervention and is driving intensive mechanistic studies of this system. These studies include the characterization of the periplasmic domain of TolA protein from several bacterial species including *Pseudomonas aeruginosa* (*29*), *E. coli* (*30*), and *Vibrio cholerae* (*31*). In addition, the structure of the corresponding domain of *E. coli* TolA has been determined in complex with the N-terminal domain of g3p phage (*30*) and with the colicin A (*32*). However, the structure of full-length TolA remains uncharacterized. Similarly, the structures of the putative periplasmic

[1]Department of Microbiology, Immunology, and Infectious Diseases, University of Calgary, 3330 Hospital Drive NW, Calgary, Alberta T2N 4N1, Canada. [2]Center for Structural Biology of Infectious Diseases (CSBID), Chicago, IL 60611, USA. [3]Department of Biophysics, University of Texas Southwestern Medical Center, Dallas, TX 75390, USA. [4]Ligo Analytics, 2207 Chunk Ct., Dallas, TX 75206, USA. [5]Department of Biological Sciences and Centre for Molecular Simulation, University of Calgary, Calgary T2N 1N4, Canada. [6]Department of Chemical Engineering and Applied Sciences, University of Toronto, Toronto, Ontario M5S 3E5, Canada. [7]Department of Biochemistry, University of Texas Southwestern Medical Center, Dallas, TX 75390, USA.
*Corresponding author. Email: alexei.savchenko@ucalgary.ca

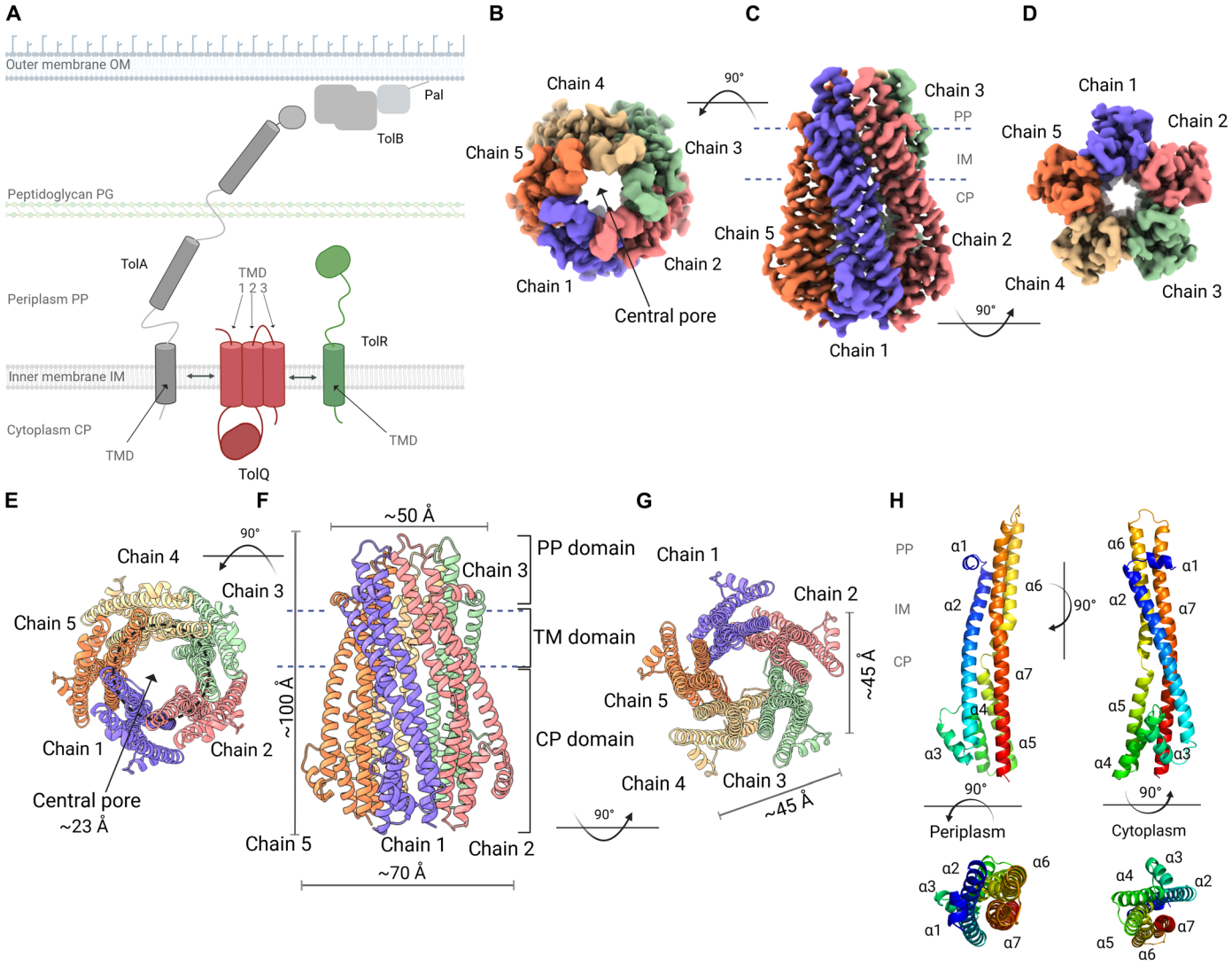

Fig. 1. Architecture and topology of the TolQ Cryo-EM structure. (**A**) Schematic overview of the Tol-Pal system for energy transduction. (**B**) Periplasmic side view of the cryo-EM map of the TolQ pentamer. (**C**) Side view of the cryo-EM map of the TolQ. (**D**) Cytoplasmic view of the cryo-EM map of the TolQ pentamer. (**E**) Periplasmic side view of the cartoon model of the TolQ pentamer. (**F**) Side view of the cartoon model of the TolQ pentamer. (**G**) Cytoplasmic side view of the cartoon model of the TolQ pentamer. (**H**) Cartoon representation of the TolQ monomer.

TolR fragments have been determined for *Haemophilus influenzae* (*33*) and *E. coli* (*12*) with nuclear magnetic resonance (NMR) and x-ray crystallography, respectively. However, the membrane-bound TolR segment has not been experimentally characterized at atomic resolution. TolQ is the only component of the TolQ-TolR-TolA subcomplex for which no experimentally derived atomic structures have been available. Recently, a cryo–electron microscopy (cryo-EM) reconstruction of the TolQ-TolR subcomplex from *E. coli* was reported (*34*). It revealed 5:2 stoichiometry for the TolQ-TolR subcomplex with transmembrane helices of TolR dimers located inside the TolQ pentamer. However, the resolution of obtained data (the 4.3-Å overall resolution of reconstruction for the complex and 4.7-Å resolution for the TolR component) did not allow for modeling TolQ-TolR interactions.

The model for the molecular mechanism of the Tol-Pal system has been proposed on the basis of the flagellar motor system MotA-MotB and nutrient transport system ExbB-ExbD, the components of which share sequence similarly with TolQ and TolR (*1*, *11*, *35*). Recent cryo-EM and x-ray crystallographic studies identified 5:2 stoichiometry for both systems, with five monomers of MotA/ExbB surrounding the transmembrane part of two MotB/ExbD molecules (*36*–*39*). On the basis of sequence similarities with MotA-MotB and ExbB-ExbD systems, the TolQ-TolR is expected to operate as the stator-rotor motor (*40*). In such a system, stators use PMF for the rotary motors, while energy provided to the motor generates torque applied to the rotor. This model has been best demonstrated in the MotA-MotB system, where the MotB acts as a stator. However, it is less certain whether the homologous components of the other two systems adopt the same mode of action.

Here, we determined a 3.02-Å cryo-EM single-particle reconstruction (SPR) structure of the full-length TolQ in apo form and a 3.34-Å cryo-EM structure of the TolQ-TolR complex from *Acinetobacter*

baumannii. *A. baumannii* is one of the most dreaded and clinically important Gram-negative ESKAPE (*Enterococcus faecium*, *Staphylococcus aureus*, *Klebsiella pneumoniae*, *A. baumannii*, *P. aeruginosa*, and *Enterobacter* spp.) pathogens causing a broad-spectrum nosocomial infection mainly among patients admitted to intensive care units (*41*–*44*).

Our findings offer experimentally derived, high-resolution structural models of both TolQ and the TolQ-TolR complexes. These models provide insights into potential mechanisms of proton translocation and force generation within the Tol-Pal system, serving as a reference for analyzing force generation in other 5:2 stator-rotor systems. In addition, they provide the molecular framework for the rational design of inhibitors against a vital molecular complex conserved across Gram-negative bacteria.

RESULTS

Molecular architecture of TolQ pentamer

As an initial step in the structural characterization of Tol-Pal system components in *A. baumannii*, we pursued the structural characterization of the TolQ protein. The corresponding gene was cloned and recombinantly expressed in *E. coli* (see Material and Methods for details). TolQ protein was purified from the membrane fraction of the cell lysate by the combination of affinity and size exclusion chromatography (fig. S1, A to D). Once purified, TolQ protein was reconstructed using amphipol polymers. According to mass photometry analysis (fig. S1D), solubilized TolQ protein formed homogeneous particles having mass higher than 100 kDa thus amenable to analysis by cryo-EM SPR.

The TolQ sample was biochemically and conformationally homogenous and generated well-behaving cryo-EM grids. Upon data acquisition, two-dimensional (2D) classification of selected particles revealed clear features of pentameric stoichiometry (fig. S2A). After 3D reconstruction with C5 symmetry, we obtained a 3.02-Å molecular density map (fig. S2, B to D, and table S2). The analysis of the map revealed five molecules of TolQ forming a pentameric assembly of ~100 Å long with ~70-Å diameter (Fig. 1, B to D), stabilized by a ring of A8-35 amphipol visible at lower contour density map at TMD region (fig. S3, A to C). To facilitate the comparative analysis, we named the chains in TolQ pentamer following nomenclature reported in previous studies for the TolQ homolog MotA (*38*) with chain 1 (see Fig. 1, B to F) corresponding to chain A in Protein Data Bank (PDB) structure 6YKM and so on.

According to our analysis, TolQ protomers contain seven α helices (Fig. 1H). The N-terminal α1 helix is positioned along the periplasmic surface of IM. The α2 helix spans the IM forming the first transmembrane helical region (TMH1) and extends into the cytoplasm. The α2 helix is followed by two cytoplasmic, relatively short, α3 and α4 helices. Cytoplasmic α5 helix loops back to the IM and is followed by α6 helix, corresponding to TMH2, which spans the membrane back to periplasmic space. The C-terminal and the longest α7 helix spanning ~100 Å forms TMH3. All helices are connected via relatively short loops. In our structure, the outer surfaces of TMH1 and TMH2 interact directly with amphipol, while TMH3 forms the inner surface of the TolQ central pore. This central tunnel has a circular opening of ~23 Å in diameter at the periplasmic side (Fig. 1E). The surface buried by interactions between two TolQ monomers is 1229 to 1234 $Å^2$ per each interface (table S1), with both periplasmic and cytoplasmic segments of TolQ also contributing to interactions (Fig. 1, E to G). A small gap exists between adjacent protomers on the periplasmic side (fig. S4).

According to Foldseek server (*45*), our *Ac*TolQ protomer structure is the most similar to the structure of ExbB from *E. coli* (PDB: 6TYI) and *Serratia marcescens* (PDB: 7AJQ) with root mean square deviation (RMSD) of 1.60 Å over 193 Cα and 2.39 Å over 159 Cα atoms, respectively. The second closest structure is flagellar stator protein MotA from *Aquifex aeolicus* and *Bacillus subtillis*, although this protein's protomers contain an additional cytoplasmic α helix lacking in TolQ (*38*, *46*). Both MotA (PDB: 8GQY) and ExbB (PDB: 6TYI and/or 6YE4) form pentameric symmetrical structures with the pore entrance from periplasmic side, similar to TolQ apo structure presented here (fig. S5, A to C).

Cryo-EM structure of TolQ-TolR complex

For structural characterization of *A. baumannii* TolQ protein in complex with TolR, TolQ and TolR genes were cloned and coexpressed using a tandem promoter vector system in *E. coli* (see Material and Methods for details). After purification using affinity and size exclusion chromatography, the fraction corresponding to the TolQ-TolR complex (fig. S1, B and C) was further analyzed by mass photometry. This analysis suggested that TolQ-TolR complex was larger than TolQ pentamer by ~30 kDa, which would correspond to the TolR dimer (fig. 1D). Cryo-EM SPR of TolQ-TolR complex confirmed 5:2 stoichiometry (Fig. 2, A to H). We will refer to this complex hereafter as *Ac*TolQ-TolR. The reconstruction of *Ac*TolQ-TdR reached overall resolution of 3.34 Å with C1 symmetry imposed (figs. S5, A to F, and S2).

Comparison of TolQ protomers conformations in apo and TolR-bound structures using PyMol revealed modest rearrangements reflected in very low RMSD value (0.50 to 0.82 Å) between TolQ protomers in both structures over 215 Cα atoms (Fig. 3A). However, superimposing tertiary structures, we observed a shift in the overall position of chain 1 in *Ac*TolQ versus AcTolQ-TolR structures to maximum of 9.32 Å at periplasmic side of the complex (Fig. 3, B and C). As a result, TolQ pentamer's central pore in the complex structure underwent the shape change from round to oval (Fig. 2B) with ~30 Å in the widest diameter accommodating the TMHs of TolR dimer inside the pore (Figs. 2, G and H, and 3, B and C). The average variation for superimposed TolQ pentamers in apo and TolR-bound structures was 1.91 Å. The analysis of interface areas between protomers calculated by PISA (*47*) highlights the asymmetry between apo and bond TolQ forms in more detail (table S1). While interface area levels are equal (~1200 $Å^2$) between TolQ protomers in the apo form, the interface area between TolQ chains varies greatly (755 to 1439 $Å^2$) in the *Ac*TolQ-TolR complex with C1 symmetry. The largest interface areas are between chains 1-2, 2-3, and 4-5 of TolQ. The wider gap between chains 3-4 and 5-1 results in smaller interface areas 755 and 823 $Å^2$, respectively (table S1).

*Ac*TolQ-TolR structure revealed the position of the N-terminal portion of TolR, which, according to our knowledge, has evaded to be experimentally visualized before. The N-terminal segments of both TolR protomers localize to the cytoplasmic chamber formed by TolQ pentamer and do not have a defined secondary structure for the region before the transmembrane helix (TMH) that starts at the residue Tyr^{25}. TolR N-terminal segments corresponding to residues Gly^{7} to Ser^{45} and Phe^{9} to Ser^{45} at the N terminus of both TolR protomers are well resolved in obtained complex structure. Such positioning of TolR N termini inside the TolQ pentamer in our model

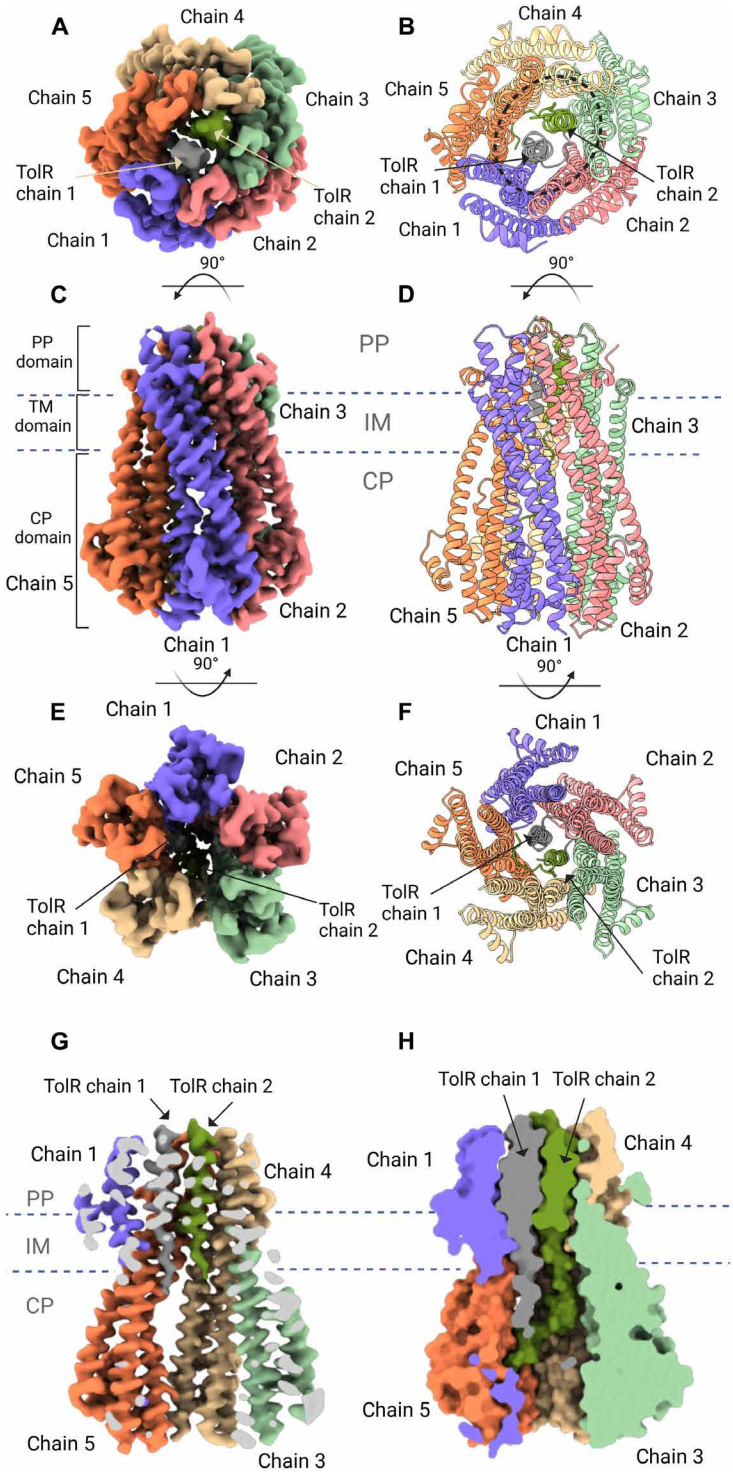

Fig. 2. Architecture and topology of the TolQ-TolR complex cryo-EM structure. (**A**) Periplasmic side view of the cryo-EM map of the TolQ-TolR 5:2 complex. (**B**) Periplasmic side view of the cartoon model of the TolQ-TolR 5:2 complex. (**C**) Side view of the cryo-EM map of the TolQ-TolR 5:2 complex. (**D**) Side view of the cartoon model of the TolQ-TolR 5:2 complex. (**E**) Cytoplasmic view of the cryo-EM map of the cryo-EM map of the TolQ-TolR 5:2 complex. (**F**) Cytoplasmic side view of the cartoon model of the TolQ-TolR 5:2 complex. (**G**) Side view of cryo-EM map of TolQ-TolR complex with the front of the complex removed. (**H**) Side view of TolQ-TolR complex surface representation of the model with the front of the complex removed.

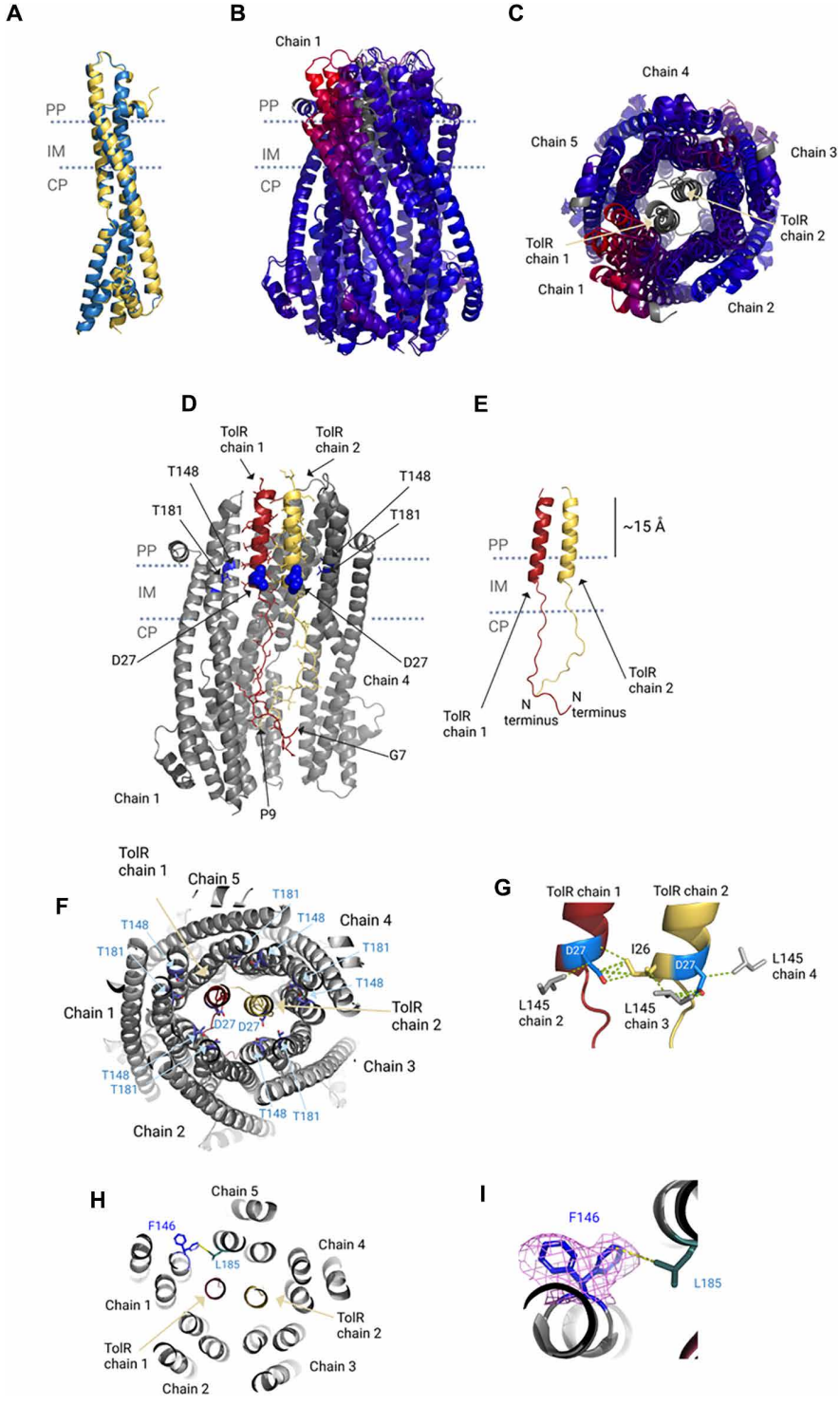

Fig. 3. Arrangements of TolQ and TolR protomers in the complex. (**A**) The superimposed TolQ protomers from TolQ (blue) and TolQ-TolR (yellow) cryo-EM structures. (**B**) The superimposed pentameric TolQ and 5:2 TolQ structures colored by RMSD, side view. Dark blue is good alignment; higher deviations are red. Residues not used for alignment are colored gray. (**C**) The superimposed pentameric TolQ and 5:2 TolQ-TolR structures colored by RMSD, periplasmic side view. Dark blue is good alignment; higher deviations are red. Residues not used for alignment are colored gray. (**D**) Cartoon representation of TolR TMD and N terminus solved structure relative to the IM, side view. (**E**) Colocalization of functionally important TolR residues (blue spheres) and its surrounding environment made by TolQ residues (blue cartoon and sticks representation), side view. TolQ chain 2 is eliminated for clarity. (**F**) Colocalization of functionally important TolR residues and their surrounding environment made by TolQ, periplasmic view with the periplasmic part cut off for clarity. (**G**) Key TolR residues D27 (blue) interactions within 3.0 to 3.8 Å distances. (**H**) TolQ chain 1 F146 side chain double conformation in TolQ-TolR structure, slab view from the periplasm. (**I**) Zoomed TolQ chain 1 F146 side chain double conformation in TolQ-TolR structure with electron density depicted in magenta.

contradicts the report that proposed for this portion of TolR to be exposed to cytosol (*48*). This orientation positions the resolved N terminus of TolR, which is composed by mostly positively charged residues against the large electronegative chamber formed by TolQ pentamer (Fig. 3E and fig. S8, C to F).

Following the segment lacking secondary structure, corresponding to the residues Tyr^{25} to Ser^{45}, each TolR protomer forms the α helix spanning the pore of TolQ pentamer and extending 15 Å beyond IM into the periplasmic side (Fig. 3D and fig. S7). The portion of TolR inside TolQ pentamer is accommodated by the oval-shaped periplasmic side of the TolQ central pore, which is lined with mostly negatively charged residues facing the periplasm side (fig. S8, A and B). The interface between TMHs in the TolR dimer buries an area of ~600 $Å^2$. This interface is almost exclusively hydrophobic (fig. S8, C to F) with six and eight residues from TolR chain 1 and chain 2, respectively, contributing over 20 nonbonding interactions (fig. S9). The N-terminal segment of TolR is connected to the C-terminal periplasmic domain via a flexible linker formed by residues Gly^{46} to Ala^{66}, which are not visible in the complex structure obtained. The C-terminal portion of TolR is referred to in the literature as the PG binding domain (PGBD) (*12*). The PGBD's shape was determined to a very low resolution in *Ac*TolQ-TolR, indicating substantial movement of the domain (figs. S6A and S7). The low-resolution map obtained for this portion of TolR agrees with previously determined crystal and NMR structures of this domain (*12*, *33*), which can be confidently modeled into it.

The general architecture of *Ac*$TolQ_5$-$TolR_2$ complex shares common features with the architecture of analogous subcomplexes from ExbB-ExbD and MotA-MotB systems (*37*, *38*). However, the α-helical regions of two TolR protomers in the *Ac*$TolQ_5$-$TolR_2$ complex are related by translational symmetry rather than by rotational symmetry observed in these systems (Fig. 3, E to G). To investigate the molecular determinants responsible for the observed differences, we pursue detailed comparative analysis of the transmembrane regions in these complexes (Fig. 4, A to F).

In *Ac*$TolQ_5$-$TolR_2$ complex, the two TMHs of TolR protomers are congruent to each other and reside in a parallel, side-by-side manner, with each amino acid in chain 1 aligned with its counterpart in chain 2. This arrangement reflects a form of translational symmetry, where chain 2 could be visualized as a translated copy of chain 1 along an axis that runs perpendicular to the length of the TMHs (Fig. 4, A and D). As a result, within ^{25}YIDVMLVLLVIFMVTAPM^{42} regions of TolR protomers, the mean distance between Cαs of equivalent residues was around 9.9 Å with only small (0.7 Å) deviations (Fig. 4B). The interactions between TolR protomers in this region are predominantly hydrophobic, with a number of residues including $Ile^{26,35}$, $Val^{22,28,34}$, $Leu^{32,33}$, Met^{39}, Tyr^{25}, and Phe^{36} from each chain engaging in nonpolar contacts (Fig. 4C). The symmetric arrangement of these residues across the dimer interface of TolR would reinforce the stability of the *Ac*$TolQ_5$-$TolR_2$ complex, making this interface potentially crucial for the functional assembly of this complex.

In contrast, in the structures of $ExbB_5$-$ExbD_2$ and $MotA_5$-$MotB_2$ complexes, the protomers of TolR paralogs ExbD and MotB are arranged in rotational symmetry when in complex with TolQ paralogs ExbB and MotA (Fig. 4, E and F). This analysis suggested that despite overall similarity, the TolQ-TolR system may be capable of dynamic movements discrete from those previously suggested for other similar molecular systems (*38*, *49*).

Analysis of TolQ-TolR interactions

Atomic resolution cryo-EM SPR enabled detailed analysis of interactions between *A. baumannii* TolQ and TolR proteins and interpretation of these interactions in context of Tol-Pal system cellular activity based on results of previously conducted biochemical or genetic experiments (*1*, *15*, *17*–*19*, *23*, *48*). Specifically, the analysis of TolQ-TolR systems in *E. coli* and *S. typhimurium* identified a number of mutations critical for the function and interactions between these proteins (*1*, *15*, *17*–*19*, *23*, *48*). Since the primary sequences of these proteins show substantial similarity with *A. baumannii* TolQ and TolR (46% of sequence ID in case of TolQ), we investigated the role of corresponding residues in *Ac*$TolQ_5$-$TolR_2$ structure (Fig. 5A).

The single mutations of residues corresponding to Asp^{27} in *A. baumannii* TolR or Thr^{148} and Thr^{181} residues in *A. baumannii* TolQ result in OM destabilization phenotypically comparable to that observed for *tol* operon deletion in *E. coli* (*23*). This residue colocalizes with Thr^{148} and Thr^{181} in one copy of *Ac*TolQ-TolR at the distance that would allow for transient interactions between these residues (Fig. 3, E and F). A similar arrangement of the corresponding residues has been observed in ExbB-ExbD and MotA-MotB complex structures (*37*–*39*). Because of the asymmetric position of TolR dimer inside the TolQ pentamer, the Thr^{148} and Thr^{181} residues of each TolQ protomer form multiple interactions with TolR. Specifically, Thr^{148} and Thr^{181} in TolQ chain 1 form nonbonded contacts with Met^{29} and Ile^{26} from TolR chain 1, respectively (fig. S10); Thr^{181} in TolQ chain 5 forms hydrogen bonds and nonpolar contacts with Tyr^{25} in TolR chain 2 (fig. S11). In addition to the interactions mentioned above, the Asp^{27} from chain 2 of TolR along with Ile^{26} are also within nonbonding contact distances (3.0 to 3.8 Å, respectively) from Leu^{145} residues in the three adjacent TolQ protomers, chains 2, 3, and 4 (Fig. 3G).

Notably, we observed the double conformation of the Phe^{146} located in TMH2 of TolQ chain 1 in the area with the widest distance between TolQ protomers due to asymmetry (Fig. 3H). One possible explanation for the conformational changes interrupting contacts between TolQ protomers could be the requirement of such alterations for TolR entry. According to the electron density map, the side chain of Phe^{146} either freely points outside the channel or turns toward the TMH2 of the next TolQ protomer chain 5, forming two nonbonding contacts with Leu^{185} (Fig. 3I). The "pointing out" conformation of the Phe^{146} phenyl group was only detected when TolR dimer was present inside TolQ. Similar to Phe^{146} residues in apo $TolQ_5$ (fig. S12), the Phe^{146} residues of the rest four TolQ protomers point toward TMH2, contributing to the interaction interface between TolQ protomers in the *Ac*$TolQ_5$-$TolR_2$ structure (fig. S13).

Individual substitution of several conserved TolQ residues has been shown to substantially alter its cellular function. Specifically, the Pro^{190}Val, Glu^{176}Gln/Leu, Ala^{155}Glu, Gly^{144}Ala, Gly^{147}Ala, Gly^{151}Ala, and Leu^{185}Cys mutations in *E. coli* TolQ protein resulted in crucial cell envelope defects (*18*, *23*). According to *Ac*$TolQ_5$-$TolR_2$ structure, the proline oxygen atom of Pro^{190} forms a main-chain polar contact with the nitrogen atom from Ala^{194}, which stabilizes α-helical structure of TolQ's protomers' TMH3. Substituting Pro^{190} to a Val would extend the distance between the two interacting atoms from 2.9 to 3.4 to 3.5 to 3.6 Å, potentially affecting each protomer's folding in TolQ pentamer. TolQ's Glu^{176} forms from one to four main-chain polar contacts stabilizing the helical architecture in TMH3 of each protomer. The Glu^{176}Gln substitution either fully abrogates main-chain polar bonds or reduces their number (chains 1, 3, 4, and 5), thus

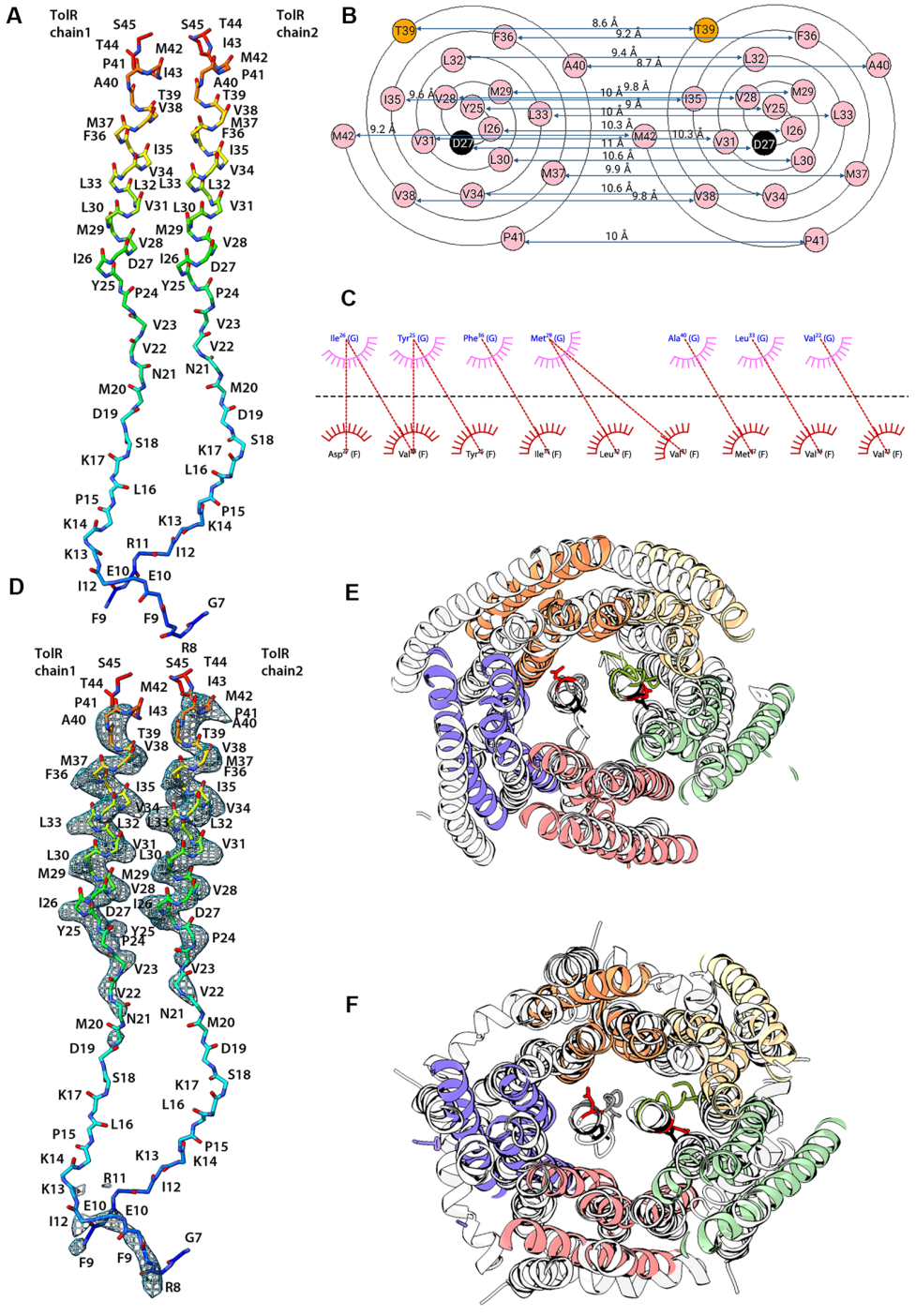

Fig. 4. Translational relations of residues in TolR TMHs in TolQ-TolR structure. (**A**) TolR chain 1 and chain 2 colored in rainbow backbones, side view. (**B**) Wenxiang diagrams for both TMHs of TolR protomers with distances between Cα. 2D depiction of TolR TMHs regions—^{25}YIDVMLVLLVIFMVTAPM^{42}—highlights the predominantly hydrophobic core of residues with the distances reflecting the spatial separation between amino acids in the interacting TolR chains 1 and 2. Residue types: The black color depicts acidic residues. The pink color depicts hydrophobic residues. The orange color depicts polar residues. (**C**) Depiction of interactions in TolR chain 1 (F) and chain 2 (G) helices using LigPlot+. Arcs show hydrophobic interactions and, in addition to arcs, hydrophobic bonds with specific residues (dashed red lines). (**D**) TolR chain 1 and chain 2 colored in rainbow backbones with an electron density map depicted as isomesh. Side view. (**E**) Depiction of *Ac*TolQ-TolR (colored) and *Ec*ExbB-ExbD (uncolored, PDB:6TYI) cryo-EM structures aligned by TolR/ExbD TMHs regions (chain 2 or G for TolR). Periplasmic view of the models with the back and front of the complexes removed. Translationally related residues of aspartic acid of TolR are colored in black, while rotationally related residues of aspartic acid of ExbD are colored in red. (**F**) Depiction of TolQ-TolR (colored) and *Campylobacter jejuni* MotA-MotB (uncolored, PDB:6YKP) cryo-EM structures aligned by TolR/MotB TMHs regions (chain 2 or G for TolR). Periplasmic view of the models with the back and front of the complexes removed. Translationally related residues of aspartic acid of TolR are colored in black, while rotationally related residues of aspartic acid of MotB are colored in red.

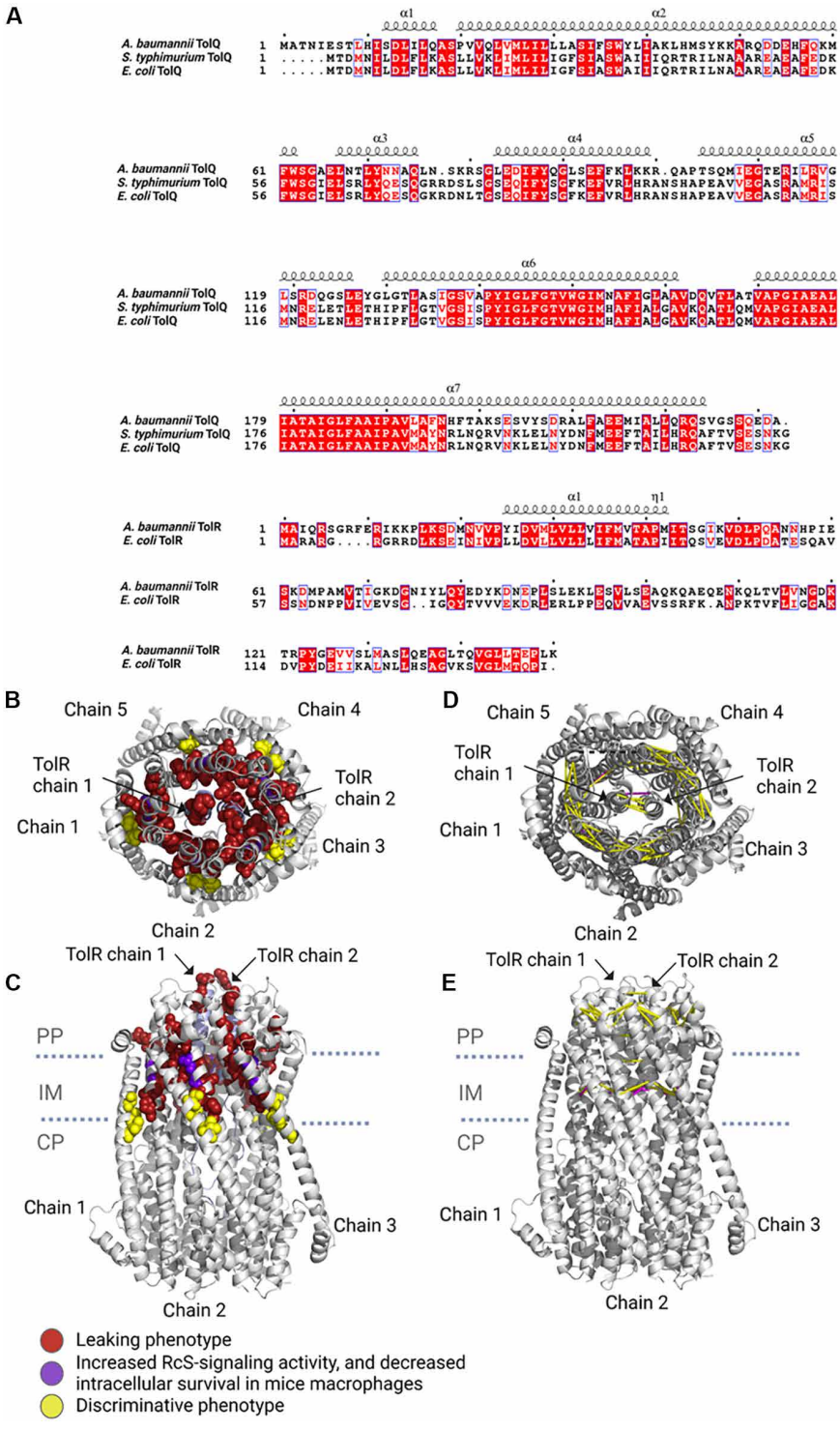

Fig. 5. Validation of *Ac*TolQ-TolR structure by prior functional data. (**A**) Sequence alignment of TolQ and TolR in species for which point mutation studies have been conducted. The mutated residues are plotted as spheres on the *Ac*TolQ-TolR structure (gray) on the position of the Cα atoms of homologous residues in *E. coli* and *S. typhimurium* as periplasmic. Sequence alignment was conducted using ClustalW and ESPript (*90*). Letters in red stand for highly conserved but not necessarily identical residues. Top periplasmic view (**B**) and side (**C**) view. (**D** and **E**) Representation (shown as dotted yellow lines between the homologous Cα atoms) of *E. coli* TolQ and TolR residues that can be cross-linked when they are mutated to cysteines. The dotted purple lines correspond to in vivo cross-linking from the prior data and the protomeric nonbonding contacts we observed in *Ac*TolQ$_5$-TolR$_2$ structure.

affecting the interactions of this residue with TMH3. Glu^{176}Leu substitution would have a milder effect on the main-chain polar bonds. However, the shorter side chain of leucine would fully abrogate interactions of this residue with TMH3. Ala^{155} is involved in main chain polar bonds with Leu^{159} and Gly^{151}, which stabilize the position of TMH2. When substituted with Glu, the long negatively charged side chain at this position will promote a substantial van der Waals overlap resulting in multiple clashes with residues of TMH3 from the same TolQ protomer (chains 1, 2, and 4 of TolQ). Gly^{144}, Gly^{147}, and Gly^{151} are located at the pore forming TMH2 of TolQ. Gly^{144} maintains main-chain polar interactions within the same protomer with Thr^{148} and Ala^{140} 2.9 to 3.1 Å in length. Substitution of Gly^{144} by Ala will result in either abrogation of contact with Ala^{140} and/or elongation of the existing contact distance with Thr^{148} in adjacent protomers. Gly^{147} faces intra-protomeric TMH1 of TolQ and provides polar interactions with Gly^{151} and Ile^{143}. The effect of the Ala mutation of this residue mutation may be explained by the loss of conformational flexibility of TMH2 necessary to accommodate the TolR helices. Leu^{185} is located at TMH3 of TolQ and is part of hydrophobic interface between TolQ protomers. A cysteine at this position would introduce a sulfhydryl group abrogating multiple nonpolar bonds and thus dramatically affecting the protomer packing of TolQ pentamer.

The substitutions of Ala^{180} or Gly^{184} equivalent residues in *S. typhimurium* TolQ by a Val or an Asp, respectively, increases RcS-signaling activity and suppresses intracellular survival in C57BL/6 mice macrophages during bacteremia (*22*). Gly^{184} is located in TMH3 of TolQ and is proximal to TMH2 of the same protomer. The substitution of Gly^{184} to Asp will cause clashes with TMH2 as well as with TMH1 residues. In turn, the Ala^{180} forms main-chain polar contacts with Ala^{177} and Gly^{184}. Mutation of Ala^{180} to Val will introduce multiple clashes with residues from TMH2 from the same protomer.

Cysteine substitutions of Ser^{33}, Ser^{36}, or Ile^{40} residues in TolQ result in colicin- and deoxycholate-sensitive phenotype (*18*). These three residues are located in the IM region of TMH1 with side chains facing TMH2 or TMH3 of the same TolQ protomer (Fig. 5, B and C). The modeling of Cys at the Ser^{33} position resulted in clashes with residues from TMH3 in each protomer of TolQ. Ser^{36} to Cys mutation will result in clashes with multiple residues from TMH2, TMH1, or TMH3, and abrogation of polar contacts with Ala^{32} and Ser^{33}. While the Ile^{40}Cys mutation does not produce obvious clashes, its discriminative effect may be explained by its location within Ser^{33}-Ala^{41} TolQ region interacting with TolA.

In TolR dimer packed inside TolQ pentamer, the Ala^{40}'s side chain faces either TMH3 of the TolQ protomer or toward the chain 1 of TolR, where it forms polar contacts with Phe^{36} and Ile^{43}. Mutation of this residue to a Val will cause clashes with TolR's chain 2 and the residues from TolQ protomer. Pro^{41} residue is located at the extremity of TMD of TolR facing periplasm. Substitution of this residue by a Val introduces multiple clashes with TolQ residues belonging to chains 2 and 3. Pro^{24} is located at the border of the disordered N terminus region of TolR and well-ordered helical TMD. In TolR chain1, Pro^{24} forms nonbonding contacts with Tyr^{145} of TolQ's chain1. The Pro^{24}Leu mutation will abrogate interaction with Tyr^{145} and will introduce multiple clashes with residues from TolQ chain 2 and Ile^{26} from the TolR's chain 1. Furthermore, in TolR's chain 2, this mutation creates multiple clashes with residues from TolQ's chain 4.

As mentioned above, TolR's Asp^{27} is expected to play a critical role in the proton pathway. Substituting this negatively charged amino acid to an Ala or a Cys will sabotage such function. Mutation of this residue to glutamic acid will also be detrimental. In TolR chain 1, the Asp^{27}Glu mutation introduces multiple clashes with Leu^{145} from TolQ's chain 2 or Pro^{24} from the same TolR protomer due to its extended side chain.

The analysis of *Ac*TolQ$_5$-TolR$_2$ structure also facilitated the interpretation of previously published in vivo cross-linking experiments to map the interface between these proteins in the complex (*17*, *18*). Following these previous studies, the residues identified as proximal belong to TolQ helices line at the inner surface of the channel (Fig. 5, D and E). However, the cross-linking observed between residues of chains 1 and 5 of TolQ protomers is not supported by our structural model of *Ac*TolQ-TolR due to the abovementioned asymmetry introduced by the binding of TolR dimer in the complex. The in vivo cross-linking studies were conducted for TolR (*17*) and TolQ (*18*) individually. Therefore, the observed discrepancy may be due to the presence of apo versus TolR-bound TolQ in bacterial cell. The cross-linked pair of residues Tyr^{142}-Ile^{189} of TolQ and Val^{23}-Val^{23} of TolR correspond to the inter-protomeric nonbonding contacts we observed in *Ac*TolQ$_5$-TolR$_2$ structure (Fig. 5, D and E, and fig. S9).

Evaluating *Ac*TolQ$_5$-TolR$_2$ structural plasticity and permeability by MD

Using the obtained *Ac*TolQ$_5$-TolR$_2$ structure, we applied in silico molecular dynamics (MD) approach to gain molecular insight into the possible structural fluctuation of this complex in the context of bacterial membrane. The stability of the simulated *Ac*TolQ$_5$ and *Ac*TolQ$_5$-TolR$_2$ structures was maintained throughout the duration of the microsecond-simulation timescale. No substantial structural rearrangements were observed in either *Ac*TolQ pentamer or *Ac*TolQ-TolR heteroheptamer in this experimental setup. The final structural models obtained from the simulation studies closely resembled the model derived from cryo-EM studies (Fig. 6, A to F). Analysis of the root mean square fluctuations indicated minimal structural fluctuations during the simulation (fig. S14). The TolQ$_5$-TolR$_2$ complex exhibited minor fluctuations in the terminal region, while the TolQ pentamer showed slightly higher fluctuations in the soluble cytoplasmic helix (Leu^{67}-Leu^{76}) and the adjacent loop region (Trp^{62}-Glu^{66}) in only one chain. In both cases, the transmembrane portions of the structures retained their shape. The energy landscapes calculated from the simulations were mostly flat, indicating minimal structural rearrangements in the microsecond-long MD simulations. In the TolQ-TolR complex, we did not observe any translational or rotational movement of the TolR monomers with respect to each other. We also did not observe any rotational movement of the TolR monomers with respect to the TolQ pentamer in the simulation timescale, highlighting the nonpermeable state. Throughout the simulation timescale, the Asp^{27} residues of the TolR dimers remain translationally coupled as the calculated distance between the Cγ atoms was 10.27 ± 0.4 Å. These findings suggest that TolQ$_5$ and TolQ$_5$-TolR$_2$ structures remain stable over extended time periods when analyzed in the context of bacterial membrane mimic and that the molecular model obtained from cryo-EM studies is representative of the native conformation of this Tol-Pal subcomplex.

To investigate the dynamic states of the *Ac*TolQ$_5$-TolR$_2$ complex and whether it could selectively allow the permeation of protons (H^+) or small cations like K^+, we calculated the pore radius along the obtained cryo-EM structure of the TolQ$_5$-TolR$_2$ complex (Fig. 6, G to I). The analysis revealed the presence of a narrow pathway in the channel spanning the transmembrane region, and constrictions were

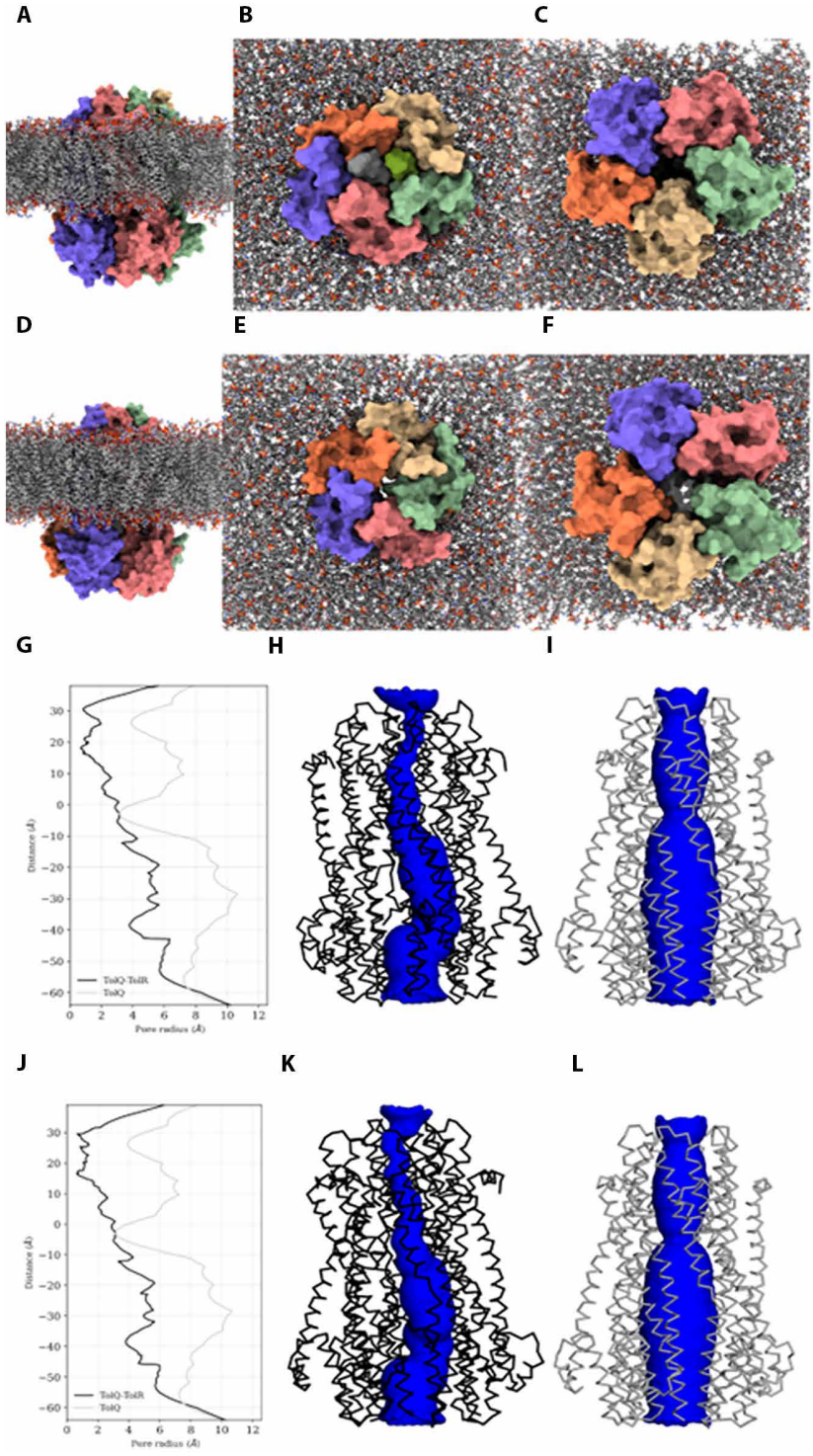

Fig. 6. Structural plasticity and pore profiles of *Ac*TolQ-TolR and apo *Ac*TolQ structures. (**A** to **C**) TolQ-TolR structure and (**D** to **F**) TolQ structure extracted after the MD simulations in native membrane environment. For clarity, only the bilayer is shown. (A and D) side view, (B and E) periplasmic view, (C and F) cytoplasmic view. Protein is shown with surface, and the lipids are shown with sticks representations. Both the structures remain largely unperturbed. (**G** to **I**) Calculated pore profiles of the cryo-EM structures and (**J** to **L**) from average structures from MD simulations. Left (G and J) shows the variation of the pore along the long-axis (membrane normal) of the proteins. Middle (H and K) and right (I and L) represent the TolQ-TolR structure and TolQ structure, respectively. Proteins are shown in ribbon, and pore profiles are shown in surface.

observed between the TolR dimer and chain 2 of TolQ. The pathway alternated between single-file water and constriction points. Three constriction points were found near the TMHs of the TolR dimer. Beyond TolR TMH, the channel path widened to a radius of at least 3 Å and maximum 6 Å in some regions, which would allow for the passage of multiple water molecules or ions. On the basis of these observations, we suggest that the overall conformation observed in the *Ac*TolQ$_5$-TolR$_2$ complex structure corresponds to a nonpermeable state of the channel. To confirm this hypothesis and explore the possibility of attaining a partially permeable state compatible with ion leakage based on the current structure, we performed and analyzed the MD simulations of *Ac*TolQ$_5$-TolR$_2$ complex. The calculated pore profile on an average structure extracted from the MD simulations remained mostly unchanged (Fig. 6, J to L), highlighting no substantial local rearrangements along the narrowest portion of the channel path. We also examined the possible dynamics of K^+ and Cl^- ions placed within the channel. The simulation confirmed the possibility of the entrance of such ions from the cytoplasmic side into the large cavity of TolQ pentamer and the possibility of K^+ ions translocating along the channel. However, our simulations also suggested that the passage of these ions will be blocked by the constriction points around the upper part of TMHs of the TolR dimer (fig. S15). These simulations also suggested that no chloride ions would be favored to enter the channel, as indicated by its electronegative nature. In summary, our simulation found no possible route for uninterrupted ion transfer in the obtained structure of TolQ$_5$-TolR$_2$ complex. To enable the passage of water and protons/ions, substantial structural rearrangement of the TolR dimer in relation to the TolQ pentamer will be necessary to allow for passage through identified constriction points. Alternatively, the passage would have to involve other structural states permissive of ion transfer.

We also conducted simulations to check the permeability of TolQ$_5$ in its apo form. Initially, we hypothesized that TolQ$_5$ would lack stability and selective permeability by protons (H^+) or potassium ions (K^+) due to the larger radius of its pore compared to canonical pores found in other ion-channels/transporters (*50*). In the absence of TolR$_2$, the radius of in TolQ$_5$ channel varies from 3.16 Å at its most narrow point to the maximum of ~11 Å at the certain segment and having a radius of ~4 Å in the periplasmic side (Fig. 6, G to I). To explore the dynamics of unbound TolQ$_5$ and assess this protein's potential for nonselective ion permeation, we conducted the MD simulations of apo TolQ pentamer.

During the simulations, the channel in TolQ$_5$ remained continuous thus confirming the possibility of this protein forming a pore in the IM. The narrowest region of the pore with a radius of 3.16 Å was at the cytoplasmic side and ~4 Å at the periplasmic side with Leu^{167} residues from all five TolQ protomers forming a constriction point. The simulations suggested rapid dewetting in specific regions of TolQ$_5$ pore, and these areas remained water molecule free throughout the simulation, even after simulating with generated pore waters (fig. S16). Dewetting initiated in the lower part of the channel, where the radius was approximately 3.16 Å, while the dehydrated portion of the channel in other regions with pore radius reaching 7.24 Å was considerably larger. Parts of the two TMHs formed the dewetting pore from each TolQ$_5$ protomer (-^{167}LATVAPGIAEALIATAIGL^{185}- from TMH3 and -^{144}GLFGTVWGIMNAFIGLAAV^{162}- from TMH2). The formation of these extensively dewetted regions would not permit the continuous passage of K^+/H^+ ions through TolQ$_5$ (fig. S17).

On the basis of the simulations, the structure of TolQ-TolR appears to have a stable conformation that corresponds to the nonpermeable state of the *Ac*TolQ$_5$-TolR$_2$, and because of the highly ordered plugging TMHs of TolR into the TolQ pore, ions are inhibited from diffusing freely across the pore. As for the apo TolQ pentamer, our simulation data suggest a nonpermeable stable apo-complex with a dehydrated pore creating a barrier for ions and waters between the cytoplasmic and periplasmic side.

Analysis of *Ac*TolQ-TolR complex dynamics

Next, we explored the dynamics of component interactions in *Ac*TolQ$_5$-TolR$_2$ complex by analyzing the heterogeneity of the particles used in the cryo-EM 3D reconstruction through 3D Variability Analysis (3DVA) (*51*). The 3DVA algorithm identifies the "variability components" of the particles in the latent space, which may be indicative of different conformational states captured in the analyzed protein sample.

Accordingly, this analysis identified multiple types of motions within the *Ac*TolQ$_5$-TolR$_2$ (movies S1 to S15). Notably, we observed that the shape of the TolQ$_5$ pore undergoes changes primarily driven by the bending motions of its protomers (movies S1 and S2). Furthermore, the rotation of a specific TolQ protomer around the perpendicular axis within the cytoplasmic region played a role in modulating pore shape in several variability components as observed in the cytoplasm and cross view of modes 1 and 2 (movies S4, S5, S7, and S8).

We observed only marginal movements in the central and upper segments of the TolR TMHs, which provided additional support for a stable H^+ nonpermeable state of the stator unit structure. In contrast, the 3DVA analysis suggested potential dynamic folding and refolding processes occurring at the N terminus of TolR in the nonpermeable state of the *Ac*TolQ$_5$-TolR$_2$ complex. The density corresponding to the disordered N terminus of TolR and the N-terminal part TMH altered between defined or undefined across all five analyzed modes (movies S3, S6, S9, S12, and S15). This recurring pattern can be indicative of this portion of TolR being in dynamic equilibrium between ordered and disordered states or accompanied and involved in the movement up and down the TolQ cavity, which results in averaging out the molecular density.

Together, 3DVA analysis revealed the bending and rotation of TolQ protomers with the magnitude of TMH movements smaller than those occurring in the cytoplasmic region. These coordinated structural changes of TolQ protomers, along with their collective interactions, have the potential to modify the shape of the pore/channel and exert an influence on its interaction with TolR dimer components.

We used Molecular Dynamics Flexible Fitting (MDFF) to extract these structures from these 3DVA intermediate maps. We fitted the structure to the intermediate maps obtained from these modes. Only one mode has notable movement that we can capture using the cryo-EM density as constraint. We observe the clear bending and rotational motion of the TolQ monomers in the cytoplasmic side (fig. S18A). We also observed the upward translational movement of the one TolR monomer (chain G) in the unstructured part (fig. S18B).

Modeling of TolQ-TolR interactions with TolA

Previous analysis (*1*, *21*, *52*) suggested direct interactions between TolQ-TolR subcomplex with the N-terminal portion of TolA protein localized to IM. Therefore, we used the obtained structure of

*Ac*TolQ-TolR to model its interaction with TolA using AF2 ColabPro server (*53*).

In the highest-ranked predicted model of TolQ-TolR-TolA complex, the single TMH of TolA spanning TM residues Phe^{9} to Leu^{33} is oriented at ABC angle with respect to the first TMH of TolQ, and the interactions between the two structural elements are stabilized by van der Waals interactions close to the cytoplasmic side of the complex (Fig. 7, A and B). Recently published Rosetta model predicted that *E. coli* TolA TMH is inserted into a TolQ groove on the exterior of the TolQ pentamer (*54*). However, cryo-EM reconstruction of the ExbB-ExbD-TonB system in *Pseudomonas savastanoi* (*Ps*ExbB-ExbD-TonB), which share substantial sequence similarity with Tol-Pal system components revealed an arrangement similar to the one suggested by our model (Fig. 7C). Analysis of *Ps*ExbB-ExbD-TonB data at a low contour level identified a single additional density, attributed to TMH of TonB, a TolA homolog, traversing the micelle located on the outer side of the ExbB-ExbD complex. This density is positioned to interact with ExbB, a homolog of TolQ, aligning with the predicted location of TonB, a homolog of TolA, determined by covariance analysis (*39*). The same arrangement between TolA and TolQ is suggested by our AlphaFold model. According to this model, residues Ala^{15}, Thr^{19}, His^{23}, and Leu^{30} belonging to TolA's TMH are involved in nonbonding contacts with Ser^{33}, Ile^{34}, Trp^{37}, Tyr^{38}, and Ala^{41} residues of the TolQ TMH1. Notably, these residues are conserved across the corresponding components of *Ac*Tol-Pal and *Ps*ExbB-ExbD-TonB systems, thus further validating the proposed model and suggesting that TolQ-TolA interactions may be following the same pattern as observed in ExbB-TonB complex structure (*39*). The polar interaction between *Ac*TolA His^{23} and *Ac*TolQ Ser^{33} was also suggested by our model, which is consistent with previous observations in *E. coli* TolA-TolQ and *P. savastanoi* TonB-ExbB systems (*39*, *54*).

Our *Ac*TolQ-TolR-TolA model suggested that TolA is forming direct interactions with the periplasmic domain of TolR. More specifically, TolA sequence following the TMH, which makes part of its periplasmic extended domain, is inserted into the C terminus periplasmic domain of TolR to form two parallel β strands (Fig. 7, A and B). This arrangement also positions the five residues of TolA (Thr^{46}-Val^{50}) between protomers in TolR dimers proximal enough to form multiple hydrogen bonds and nonbonded contacts with TolR residues. This model is somewhat reminiscent of interactions observed in recently defined crystal structures of *E. coli* ExbD-TonB periplasmic fragment complex, where ExbD, the TolQ homolog, captures one copy of the TonB peptide via β strand recruitment (*55*, *56*). However, the superimposition of this crystal structure with the obtained model of *Ac*TolQ-TolR-TolA highlights a substantial difference in the orientation of TonB versus TolA interacting regions. Thus, the experimental validation of proposed *Ac*TolQ-TolA interactions is required.

DISCUSSION

The components of the Tol-Pal system (TolA, TolB, TolQ, TolR, and Pal) assemble into complexes that, depending on their composition, are anchored at the IM and/or OM and interact with PG. The structural transitions of these complexes are driven by the electrochemical gradient that forms between the cytoplasm and periplasm. The TolQ-TolR-TolA subcomplex is considered to represent a motor that generates rotary force driven by the electrochemical gradient. The rotary force is then transferred by TolA to reorganize other subcomplexes of the Tol-Pal system. There are unanswered questions about how TolQ-TolR generates torque and how the torque force is used by TolA. The torque generation is presumably conserved across other reported 5:2 motors; however, whether the force is used in an analogous way after it is generated remains to be determined.

The structures of TolQ-TolR complex in comparison to the TolQ pentamer are used as the basis for the TolQ-TolR-TolA activation mechanism proposed here, which has distinct features not considered in previously published models. The earlier models were based on the similarity of the TolQ-TolR system to two other systems: the

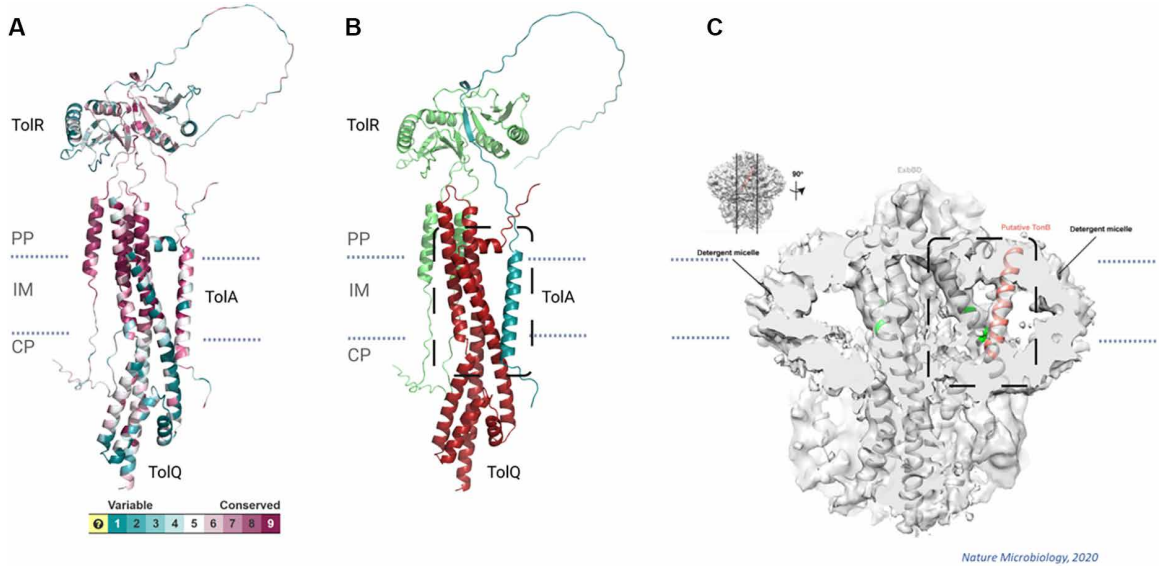

Fig. 7. Interaction of *Ac*TolQ-TolR with TolA. (**A**) AlphaFold2 model colored by residue conservation. (**B**) AlphaFold2 model colored by subunit (TolQ, red; TolR, green; TolA, blue). (**C**) Low-resolution cryo-EM map of ExbB-ExbD-TonB adapted from (*39*).

MotA-MotB pilus motor and the ExbB-ExbD transport system. However, the structural data presented here revealed several important features that differentiate TolQ-TolR from these homologous systems: (i) TolR helices in the TolQ pore are related to each other by translation, not by rotation, as in the homologous structures of MotA-MotB and ExbB-ExbD complexes; (ii) the TolQ pentamer in the 5:2 complex deviates from perfect fivefold symmetry in periplasmic region substantially more than in other complexes resulting in the absence of contacts between two subunits of TolQ (chain 1/A and chain 5/E in our model).

On the basis of obtained structural data, we suggest the following model for TolQ-TolR-TolA complex. In this model, TolQ pentamer is embedded in the IM, with the N-terminal fragments of two TolR molecules complexed residing inside the opening in pentameric TolQ. This portion of TolR is connected via flexible linkers to the periplasmic domains of this protein forming a dimer. The N-terminal TMH of TolA complexes with the TolQ-TolR subcomplex, with its periplasmic part also interacting with TolR. TolA is thought to extend through the periplasm and is known to interact with TolB and Pal through its C-terminal domain in a PMF-dependent manner. This assembly mechanism is consistent with previously published biochemical, biophysical, and phenotypical data.

Along with MotA-MotB and ExbB-ExbD complexes, the TolQ-TolR is expected to serve as a stator-rotor motor in the IM. Such molecular systems operate by cycling through distinct conformational states, in response to an energy input. During operation, one component of the motor rotates relative to the other. The number of cycles involved in a full 360° rotation of the stator-rotor motor depends on the intermediate conformational states. In the MotA-MotB system, 10 cycles were suggested, each leading to a rotation by 36°. However, a model with a 72° cycle has also been suggested as an alternative (*38*).

Conformational flexibility adds to complexity of molecular stator-rotor motors rotation, compared to mechanical analogs. In the case of TolQ-TolR, the TolQ pentamer (stator by engine analogy, but rotor in our drawing) does not have a perfect fivefold symmetry, indicating that it must readjust its shape during its relative rotation around TolR. The direction of the molecular rotation is not apparent from obtained structural data requiring further analysis by MD modeling that would couple proton transfer to this motor's rotation. Accordingly, the direction of rotation in our schematics was chosen arbitrarily.

TolR carries the critical proton-binding Asp^{27} residue shown to be critical for proton binding, which can operate individually or in tandem in context of the dimer formed by this protein. Accordingly, 1 or 2 protons can be transferred per rotation event. On the basis of the analysis of *Ac*$TolQ_5$-$TolR_2$ complex, we propose that the transfer of a proton (or two) generates a conformational change in the TolQ-TolR complex, resulting in a 36° rotation of TolQ, coordinated with a 180° rotation of the TolR helices within the TolQ pore. This subsequent structural state would retain the same interactions between TolQ and TolR as at the starting point while the positions of two TolR helices are being swapped. The entire complex will require another 36° rotation coupled to another (or two) proton transfer to return to the state with the same stereochemistry of TolQ and TolR interactions. Since the local chemical interactions between the TolQ and TolR helices are maintained after the first 36° rotation, the kinetics of the second step are the same as in the first step (*49*). Ultimately, the entire cycle involves a 72° rotation of the TolQ pentamer around the TolR dimer, forming a state shifted by one TolQ subunit (Fig. 8).

In each 36° cycle, the two TolR protomers may rotate either in sync or sequentially, one after the other. If they rotate in sync, it is likely that they rotate in opposite directions to preserve their contacts acting similarly to a twin-screw pump. However, the TolR helices may also rotate sequentially, with each rotation coupled to conformational or chemical events (e.g., proton transfer, changes in protonation of Asp residues, or shifts in the TolQ pentamer). In this case, rotation of both TolR helices could involve two proton transfers. The sequential rotation mechanism may generate states where the helices are related by a twofold axis, as observed in related stator-rotor complexes (*38*, *49*).

If TolR subunits rotate independently, the direction of rotation is difficult to predict, as it depends on intermediate conformational states and kinetics of the reaction. TolR could either rotate back and forth as proposed for in sync rotation or may rotate continuously in one direction. The unwinding of the connection between TolR α helices to the N terminus and C terminus in the model of continuous rotation of TolR is not necessary because peptide bond can rotate around psi angle with a moderately low energy barrier.

Assignment of specific stator and rotor roles to TolQ and TolR is hindered by substantial structural flexibility of each of these components suggested by our structural analysis. Notably, no substantial structural rearrangements were proposed for systems like MotA-MotB and ExbB-ExbD, where inner components maintain twofold symmetry, recreating equivalent structures after each 36° rotation.

The rotation of TolQ-TolR in the IM must be coupled with changes in other components of the Tol-Pal system in the IM, periplasm, and OM (Fig. 9, A to C). For a torque-generating motor, energy propagation requires that both components be anchored separately, meaning that both TolQ and TolR must be externally anchored. TolA is the protein that anchors TolQ to a structure external to TolQ (Fig. 9B). One postulated possibility is TolA's interaction with TolB, which is anchored in the OM by Pal component of this system; such interactions would create a necessary anchor for TolQ. In this model, TolR is anchored through interactions with PG. However, there is also an alternative model (*57*), in which TolA is topologically trapped by the TolR dimer, simultaneously creating both anchors, with the rotation of TolQ around TolR pulling TolA through the topological trap (Fig. 9C). Recently published ExbD (TolR homolog) structures complexed with TonB (a TolA homolog) and HasB (TonB paralog with single heme transport function) fragments (*55*, *56*) may be capturing the intermediate state leading to the formation of such topological trap. Collectively, previously reported experimental data and our analysis indicate that this system may be using either model depending on a specific function.

As discussed above, our analysis suggests that the obtained structure of *Ac*$TolQ_5$-$TolR_2$ complex corresponds to a nonpermeable conformation state (Fig. 9A). TMHs of the TolR dimer are highly ordered and embedded inside the TolQ pentamer forming a transmembrane IM channel with no ion flow. The periplasmic domain of TolR seems to be dimerized in this state as well. The periplasmic and partial IM region of one TolQ protomer is shifted to the side because of the insertion of the two TolR TMHs. Considering that PG is expected to be rigid (*58*) and that the periplasmic domain of TolR may need to bind PG for its active state (*12*), we propose a rotary mechanistic model for the TolQ-TolR complex where the TolQ pentamer rotation around TolR dimer during activated phase, similar to the ExbB-ExbD mechanistic rotary model (Fig. 9, B and C). TolR can be tethered by two possible mechanisms. One involves the attachment to the PG layer, which is in line with previously proposed model.

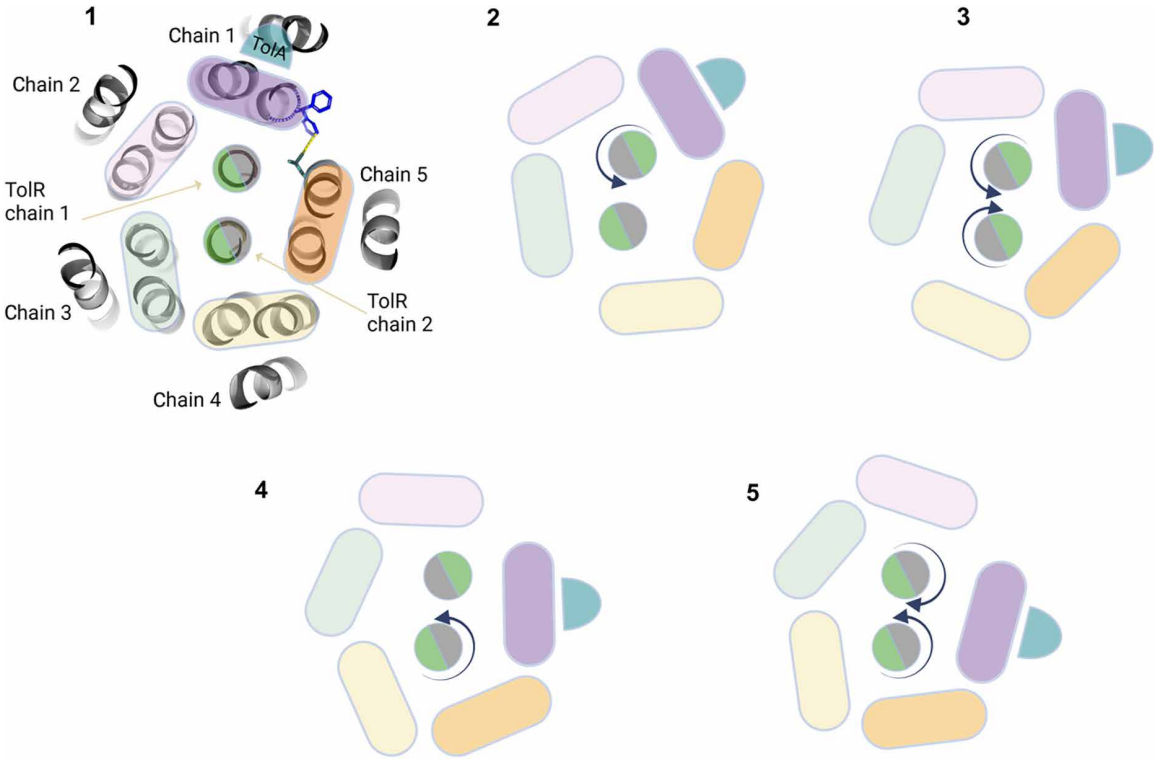

Fig. 8. Schematics of coevents during TMD rotational movements of *Ac*TolQ and *Ac*TolR protomers in IM environment. State 1 represents the TMH core of the *Ac*TolQ-TolR complex, viewed from the periplasmic side, with five TolQ chains asymmetrically surrounding two TolR dimer TMHs and TolA single TMH bond to TolQ TMH chain 1/A protomer. The actual view of *Ac*TolQ-TolR complex from the periplasmic side is overlapped for convenience. State 2, one TolR rotated 180°; TolQ rotated possibly between 0° and 36°. State 3, both TolR are now rotated 180° compared to state 1; TolQ rotated 36° compared to state 1. State 4, one TolR rotated 180° from state 3; TolQ rotated between 0° and 36° from state 3 like in step 2. State 5, both TolR rotated 180° from state 3, TolQ rotated another 36° from state 3. States 3 and 5 represent the same complex with 36° and 72° rotation of TolQ pentamer from state 1. States 2 and 4 represent possible intermediate states of the complex after 180° with rotation of each TolR protomer. Structures representing states 2 and 4 are observed in other homologs of TolQR (*37*–*39*). The direction of rotation is arbitrarily chosen. The rearrangement of uneven gaps between TolQ protomers in respect to TolR in steps 2 and 4 is unknown. It is also unclear which steps are coupled to proton transfer. Steps from 1 to 3 could translocate 1 or 2 protons. Analogously, steps from 3 to 5 could also accommodate the translocation of 1 or 2 protons.

The other possibility is that TolA is engaging the periplasmic portion of TolR dimer. Data showing a strong interaction between TolA and the C terminus of TolR homologs support the plausibility of latter model (*56*). It is also possible that both mechanisms function under different physiological conditions. The activation of the proton flow can be initialized by the Thr^{46}-Val^{50} sequence of TolA embedding into the β sheets predominantly formed by the C terminus of the TolR dimer. In this case, the TolA hairpin may need no PG pore to extend to OM to associate with TolB in its complex with Pal (Fig. 9B). However, this process may involve additional steps that need to be further investigated. According to this model, the 1.5 full rotations of TolQ protomers along with the serial rotation of TolR protomers would lead to formation of an additional space between periplasmic portions of TolR protomers. This can serve as so-called topological trap where the portion of TolA slides between two β strands of TolR initiating the pulling of the TolA helical hairpin toward the IM (Fig. 9C). We did not indicate the elongation of the flexible TolR linker between TMHs and the β sheet periplasmic domain during the activation step because the thickness of periplasm varies between bacterial species (*59*). The distance between the IM and the low-resolution density of the TolR periplasmic domain in the low-contour cryo-EM map is about 50 Å (fig. S7), which seems to be enough to reach and go through the thin PG layer.

The structure of the TolQ-TolR system from *E. coli* became available recently (*34*). However, comparative analysis of this structure with that of *Ac*$TolQ_5$-$TolR_2$ is hampered by relatively low resolution of obtained molecular density maps (the 4.3-Å overall resolution of reconstruction for the complex and 4.7-Å resolution for the TolR component). As a result, accurately assigning residues' positions in the density map was not possible, and the model was obtained by docking of the model obtained using AlphaFold server directly into the density. This atomic model does not agree well with deposited density maps (EMDB-16816). Upon inspection, we found that of the five subunits of *Ec*TolQ in the model, only three partially agree with the map, while the remaining two subunits do not. The density in these regions indicates that the reconstruction contains a mixture of structural states. This interpretation is further supported by the presence of molecular density representing a single helix that is not discussed but overlaps with both poorly resolved subunits of the AlphaFold model simultaneously.

In conclusion, here we reported the structures of TolQ-TolR protein complex from *A. baumannii*, a pathogen of substantial clinical concern. We analyzed computationally the molecular flexibility and characterized the proton sites and general flow path through this complex revealing that obtained structure appear to be in a state that does not allow for proton flow. The phenomenon of dewetting

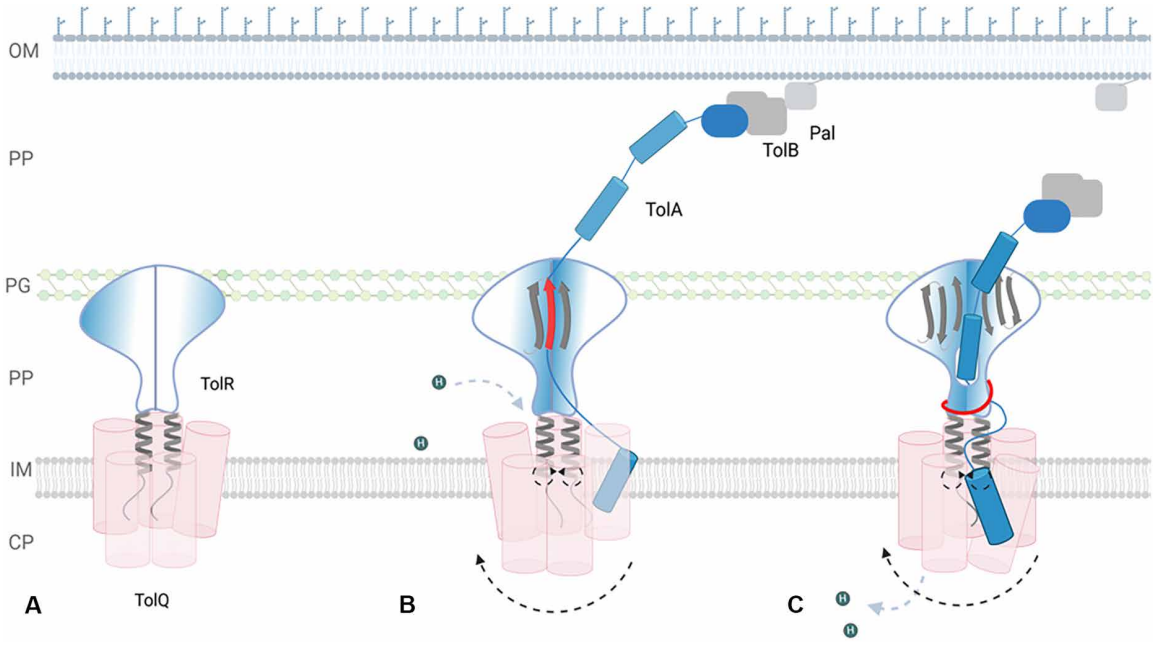

Fig. 9. Mechanistic model for the generation of Tol-Pal torque. (**A**) Structurally resolved state of asymmetric *Ac*TolQ-TolR complex. (**B**) Presumed intermediate state in the process of TolA being topologically captured by TolR periplasmic dimer (AF). (**C**) The state representing TolA being threaded through by the topological trap after serial rotation of asymmetric TolQ pentamer and TolR dimer. During this threading, secondary structure of TolA (e.g., red β strand or the α helix next to it) may be disrupted. In this state, TolA slips between two TolR straps through an unstructured hole formed between the periplasmic TolR protomers.

regions of the pore formed by TolQ protomers identified through molecular simulations holds substantial scientific interest and may serve as inspiration for the design of de novo hydrophobic pores. Obtained structural data allowed us to map the critical functional mutations in TolR and TolQ shown to disrupt the bacterial OM stability locating the structural regions that could be exploited in rational, structure-assisted development of antibacterial therapeutics. On the basis of TolQ-TolR structure, we proposed a model for TolQ-TolR-TolA interactions and discussed possible mechanisms of actions of TolQ-TolR-TolA subcomplex of Tol-Pal. These predictions await experimental validation by further structural studies. Combined, our findings bring knowledge to help further understand how molecular stator units energize vital bacterial functions, which will potentially be applicable for drug discovery.

MATERIALS AND METHODS

Protein cloning, expression, and purification

The *A. baumannii* DNA encoding the protein *Ac*TolQ (GenBank: KFC02860.1) was codon optimized for expression in *E. coli* expression systems, synthesized (Twist Bioscience), and used as the template for subcloning into pMCSG53 and pNIC-CH vectors with an N- and C-terminal 6His-tag, respectively. Both constructs had high level of expression. Therefore, we proceeded further with the construct cloned in pMCSG53 since it contained a Tobacco Etch Virus protease cleavage site enabling us to eliminate all nonspecific Ni resin binders from the samples. For the *Ac*TolQ-TolR complex, the *Ac*TolR (GenBank: HAV5244423.1) sequence was also codon optimized, synthesized (Bio Basic Inc.), and used for subcloning. Initially, we used a single-cassette-polycistronic strategy (*60*) using the abovementioned pMCSG53 vector where 6His-tag was associated with *Ac*TolQ protein. This led to higher abundance of *Ac*TolQ than *Ac*TolR in the purified sample. To overcome these technical difficulties, we applied a multi-cassette approach (*60*), where N-terminally 6His-TEVcleavage site–tagged *Ac*TolR [multiple cloning site 1 (MCS1)] and untagged *Ac*TolQ (MCS2) genes were cloned in the petDUET1 vector. Vectors were transformed into the C43(DE3)–competent cells by 60-s heat shock at 42°C and 1-hour outgrowth and plated onto LB agar selection plates. Subsequently, the single colonies of transformed cells were cultured overnight in 50-ml LB medium supplemented with ampicillin (100 μg/ml) at 37°C. The next morning, the 3, 5, or 6 liters of LB medium containing ampicillin (100 μg/ml) was inoculated with starter culture for further growth at 37°C until reaching an optical density at 600 nm of 0.6. Afterward, the culture was incubated on ice for 1 hour, followed by induction using 1 mM isopropyl β-D-thiogalactopyranoside and overnight growth at 20°C. Harvesting of cells was achieved through centrifugation, and pelleted cells were resuspended in 1x phosphate-buffered saline (PBS) (pH 7.4) and lysed using serial freezing and thawing cycles in the presence of phenylmethylsulphonyl fluoride, deoxyribonuclease 1 (20 μg/ml), lysozyme (100 μg/ml), and 0.5 mM reducing agent [Tris(2-carboxyethyl)phosphine (TCEP)]. All subsequent purification steps were carried out at 4°C. The cells were broken in a cell disruptor (Avastin) at 15,000 psi and three passes. Cell debris was spun down at 13,500*g* for 20 min. The isolated supernatant was ultracentrifuged for 1 hour and 40 min at 40,000 rpm. The pellet (crude membrane preparation) was washed using a spatula with 1x PBS with 0.5 mM TCEP and ultracentrifuged again at 40,000 rpm for 1 hour and 30 min. The isolated membrane pellet was frozen and kept at −80°C. The crude membrane preparation was solubilized with extraction buffer [50 mM Na phosphate buffer (pH 7.6), 300 mM NaCl, 20% (v/v) glycerol, 0.5 mM TCEP, and 1%

n-Dodecyl-β-D-maltoside (DDM)] for 2 hours. After ultracentrifugation (40 min and 40,000 rpm), the supernatant was incubated with 3 ml of nickel-nitrilotriacetic acid (Ni-NTA) beads (Qiagen) preequilibrated with the same buffer overnight. The next day, the beads were washed with 30 ml of wash 1 [50 mM Na phosphate (pH 7.6), 500 mM NaCl, 15% (v/v) glycerol, 0.5 mM TCEP, 40 mM imidazole, and 0.1% (w/v) DDM] and wash 2 [50 mM Na phosphate (pH 7.6), 300 mM NaCl, 10% (v/v) glycerol, 0.5 mM TCEP, 50 mM imidazole, and 0.05% (w/v) DDM] buffers and then eluted with 15 ml of the elution buffer [50 mM Na phosphate (pH 7.6), 300 mM NaCl, 5% (v/v) glycerol, 0.5 mM TCEP, 0.05% (w/v) DDM, and 300 mM imidazole]. The eluate was dialyzed overnight with TEV protease (purified in-house) in dialysis buffer [50 mM tris (pH 8.0), 300 mM NaCl, 5% (v/v) glycerol, 0.5 mM TCEP, and 0.05% (w/v) DDM]. The next day, IMAC Ni-NTA beads (Qiagen) were used for the second time where the flow-through fraction was passed for five times through the beads. The further steps of purification using various detergent environments failed to generate samples suitable for cryo-EM SPR. Therefore, other membrane protein stabilizers were tested. Amphipol A8-35 (Anatrace) resulted in the best-quality sample in our trials and was then used in large-scale purifications. Amphipol was added to the flow-through solution in 1/3 (w/w) protein/amphipol ratio, and the mixture was incubated with gentle rotation. After 4 hours of rotation, Bio-Beads (Bio-Rad) were added to the mixture in a ratio of 15 mg of beads per 1 ml of mixture volume and incubated overnight. The next day, the sample with proteins stabilized in amphipol was poured over an empty column to get rid of Bio-Beads and concentrated using 100-kDa cut-off centrifugal concentration tube (Amicon). The concentrated sample was loaded on a Superdex 200 increase 10/300 column equilibrated with detergent-free 50 mM tris (pH 8.0), 150 mM NaCl, and 0.5 mM TCEP Cryo-EM buffer. The peak fractions were collected, concentrated, aliquoted at 15 μl, flash frozen in liquid nitrogen, and kept frozen at −80°C until use. Mass photometry assay was conducted as previously described (*61*).

Grids preparation and data collection

The purified proteins samples were processed on Quantifoil R 1.2/1.3 300 Mesh Gold grids, which had been made hydrophilic through glow discharge for 90 s at 30 mA in a PELCO easiGlow system. These prepared grids were then used to create vitrified samples using a Thermo Fisher Scientific Vitrobot Mark IV, applying 3 μl of protein at 4°C and 100% humidity before blotting. Data collection was performed using a Titan Krios G2 microscope with a K3 Summit camera, without a phase plate or objective aperture, using SerialEM for automated collection and a GIF Quantum Energy Filter. Data were collected using a 300 kV Titan Krios G2 microscope equipped with a K3 Summit camera, without a phase plate or objective aperture, at a magnification of 105,000× and a pixel size of 0.834 Å. SerialEM software facilitated automated collection in beam-image shift mode, capturing nine images per stage shift across a defocus range of −1.0 to −3.0 μm, with beam-image shift compensation. The slit width of the GIF Quantum Energy Filter was set to 25 eV. Movies were dose-fractionated into 125 frames with a total dose of ~100 e^{-}/Å2.

Cryo-EM image processing and model building

For apo *Ac*TolQ, 2763 movies were imported into CryoSPARC, followed by patch motion correction using binning of 2 and patch Contrast Transfer Function (CTF) correction. Particles were first picked manually to generate templates, which was followed by template-based autopicking, resulting in 472,724 particles. Iterative 2D classification led to the selection of 246,741 particles for further processing. Ab initio reconstruction on the clean particle stack with four classes and one round of heterogeneous refinement was conducted, resulting in one class corresponding to the TolQ pentamer and three classes unrelated to TolQ. Nonuniform refinement of 215,170 particles resulted in a 3.02-Å final map in C5 symmetry, which was post-processed using DeepEMHancer to guide map interpretation. The homology model built in SwissModel using the ExbB structure as the template was used in Chimera to build the pentamer. The pentameric model was manually adjusted with rigid body refinement in Coot and then further adjusted using real-space fitting procedures. The built model was refined in Servalcat within CCPEM and validated with the MolProbity server. Model statistics can be found in table S2.

For *Ac*TolQ-TolR complex, all movies were imported into CryoSPARC followed by patch motion correction using binning of 2 and patch CTF correction (*62*). Particles were first picked using blob picker on 200 micrographs to generate initial 2D templates. Templates were created from selected 2D classes and template picking on all micrographs, resulting in a total of 3,009,251 particles. Particles were extracted with box size of 432 pixels followed by several rounds of 2D classification that yielded 465,839 clean particles. Ab initio reconstruction on the clean particle stack with three classes to separate TolQ/TolR complexes from TolQ oligomers and contaminants. The class for TolQ/TolR complex (224,768 particles) was selected for homogeneous refinement and nonuniform refinement in C1 symmetry and resulted in a resolution of 3.46 Å (*63*). The periplasmic domain of TolR was not well resolved because of its small size and high flexibility and was likely causing misalignment of the well-resolved TMD. For this reason, local refinement was performed by masking out the density from the periplasmic domain, which improved the map resolution to 3.34 Å. An initial atomic model was obtained by manually docking the AF2 model of the TolQ-TolR complex to the map using Chimera (*64*). The model was then iteratively rebuilt manually in Coot and refined using Phenix.real_space_refine and Servalcat (*65*–*70*) . Model statistics can be found in table S3.

Point mutation analysis

The mutagenesis wizard of PyMOL was used to analyze mutations mapped onto the TolQ-TolR complex structure (*71*).

MD simulation procedure

All atom MD simulations (table S4) were performed for both the TolQ-TolR 5:2 complex and TolQ pentamer. Both the complexes were embedded in a bacterial IM mimic. The membrane model consists of PPPE, PVPG, PVCL2, and POPA lipids in the following ratio PE:PG:CL:PA = 78:12:6:4; the model is consistent with other theoretical models and experimental assays in the literature (*12*, *72*–*74*). Lipids were distributed equally in both leaflets. A total of 400 lipids were used for both the systems. A water buffer of 14.5 Å is used in z dimension, with a salt concentration of 150 mM KCl. For the TolQ system, we generated pore water in the empty space of TolR dimers. The systems were generated using Charmm-GUI membrane builder (*75*–*77*). All the simulations were performed using NAMD (v 2.14) (*78*). We used CHARMM36 force field parameters for these simulations (*79*, *80*). The systems were initially minimized for 10,000 steps

with a conjugate gradient algorithm before the 6-step equilibration protocol recommend by Charmm-GUI. Later, we carried out 1-μs simulation for both systems. The simulations were carried out at 310 K. A cut-off distance of 12 Å was used, and the switch distance was set to 10 Å. Long-range electrostatics calculations beyond the cutoff were taken into account using particle mesh Ewald method (*81*). A time step of 2 fs was used for the production simulations. The temperature was controlled using the Langevin dynamics (temperature damping coefficient: 1.0), and the pressure was controlled using the Langevin piston method (*81*) (set to 1 atm, oscillation period: 50 fs, damping timescale: 25 fs). Semi-isotropic pressure coupling was used to retain the bilayer shape. Analyses were carried out using VMD (*82*), MDAnalysis (*83*), and HOLE (*84*).

3D variability assay procedure

To visualize the motion of the complex, a mask that excludes the amphipol ring around the TMD was generated. This mask and the particles in the local refinement were used as inputs for the 3D Variability job in CryoSPARC (*51*). Five modes were solved in the analysis with C1 symmetry and filter resolution of 6 Å. Results were exported using 3D Variability Display job (simple mode) with 20 frames per mode. Movies for each mode/component were generated by Chimera (*64*).

MDFF procedure

We used MDFF (*85*) to fit the cryo-EM structures to the intermediate maps obtained from the 3DVA analysis. We used CHARMM36 force field and NAMD to perform these simulations using the vacuum protocol of MDFF. The cutoff and switching distances were 9 and 10 Å. A timestep of 1 fs was used, and the temperature was set to 300 K. We applied secondary structure restraints along with cis-restraints and chirality restraints. A gscale value of 0.3 was applied. The MDFF simulations were ran for 500 ps.

AlphaFold modeling

To determine the Cryo-EM structures, the AlphaFold models of apo *Ac*TolQ$_5$ and *Ac*TolQ$_5$-TolR$_2$ were calculated using the Google Colab platform and AlphaFold2_advanced option https://colab.research.google.com/github/sokrypton/ColabFold/blob/main/beta/AlphaFold2_advanced.ipynb (*86*). The default mode of sampling options was used: num_models = 5, ptm option, num_ensemble = 1, max_cycles = 3, num_relax = 0, tol = 0, num_samples = 1. The model with the highest-ranked pTMscore was used as a template for molecular replacement. For *Ac*TolQ$_5$-TolR$_2$ heteroheptamer prediction, the 5:2 stoichiometry was included in the input. To stay within the 1400-residue limit, each TolQ protomer was 12 and 9 amino acids truncated from N and C termini, respectively.

The same approach was used to model *Ac*TolQ-TolR interaction with *Ac*TolA. To not exceed the residue limit, TolQ:TolA:TolR in 1:1:2 stoichiometry was used as input. *Ac*TolQ had no truncations in this calculation set. *Ac*TolA fragment contained the first 99 amino acids corresponding to the IM domain and the periplasmic fragment. *Ac*TolR dimer was included in full length. The structure figures were drawn with PyMOL (*71*).

Figures preparation

Figures were generated using Chimera (*64*), ChimeraX (*87*), PyMOL (*71*), VMD (*82*), HOLE (*84*), Matplotlib (*88*), PDBSum (*89*), ENDscript (*90*), PISA (*47*), R package and helixvis (*91*), and BioRender.com.

Supplementary Materials

The PDF file includes:
Figs. S1 to S18
Tables S1 to S4
Legends for movies S1 to S15

Other Supplementary Material for this manuscript includes the following:
Movies S1 to S15

REFERENCES AND NOTES

1. E. Cascales, R. Lloubès, J. N. Sturgis, The TolQ-TolR proteins energize TolA and share homologies with the flagellar motor proteins MotA-MotB. *Mol. Microbiol.* **42**, 795–807 (2001).
2. C. A. Santos, R. Janissen, M. A. S. Toledo, L. L. Beloti, A. R. Azzoni, M. A. Cotta, A. P. Souza, Characterization of the TolB-Pal trans-envelope complex from *Xylella fastidiosa* reveals a dynamic and coordinated protein expression profile during the biofilm development process. *Biochim. Biophys. Acta* **1854**, 1372–1381 (2015).
3. R. Derouiche, H. Bénédetti, J.-C. Lazzaroni, C. Lazdunski, R. Lloubès, Protein complex within *Escherichia coli* inner membrane. TolA N-terminal domain interacts with TolQ and TolR proteins. *J. Biol. Chem.* **270**, 11078–11084 (1995).
4. E. Bouveret, R. Derouiche, A. Rigal, R. Lloubès, C. Lazdunski, H. Bénédetti, Peptidoglycan-associated lipoprotein-TolB interaction: A possible key to explaining the formation of contact sites between the inner and outer membranes of *Escherichia coli*. *J. Biol. Chem.* **270**, 11071–11077 (1995).
5. J. Szczepaniak, P. Holmes, K. Rajasekar, R. Kaminska, F. Samsudin, P. G. Inns, P. Rassam, S. Khalid, S. M. Murray, C. Redfield, C. Kleanthous, The lipoprotein Pal stabilises the bacterial outer membrane during constriction by a mobilisation-and-capture mechanism. *Nat. Commun.* **11**, 1305 (2020).
6. A. J. F. Egan, Bacterial outer membrane constriction. *Mol. Microbiol.* **107**, 676–687 (2018).
7. J. Szczepaniak, C. Press, C. Kleanthous, The multifarious roles of Tol-Pal in Gram-negative bacteria. *FEMS Microbiol. Rev.* **44**, 490–506 (2020).
8. A. A. Yakhnina, T. G. Bernhardt, The Tol-Pal system is required for peptidoglycan-cleaving enzymes to complete bacterial cell division. *Proc. Natl. Acad. Sci. U.S.A.* **117**, 6777–6783 (2020).
9. P. Samire, B. Serrano, D. Duché, E. Lemarié, R. Lloubès, L. Houot, Decoupling filamentous phage uptake and energy of the TolQRA motor in *Escherichia coli*. *J. Bacteriol.* **202**, e00428-19 (2020).
10. J.-C. Lazzaroni, J.-F. Dubuisson, A. Vianney, The Tol proteins of *Escherichia coli* and their involvement in the translocation of group A colicins. *Biochimie* **84**, 391–397 (2002).
11. P. Germon, M. C. Ray, A. Vianney, J. C. Lazzaroni, Energy-dependent conformational change in the TolA protein of *Escherichia coli* involves its N-terminal domain, TolQ, and TolR. *J. Bacteriol.* **183**, 4110–4114 (2001).
12. J. A. Wojdyla, E. Cutts, R. Kaminska, G. Papadakos, J. T. Hopper, P. J. Stansfeld, D. Staunton, C. V. Robinson, C. Kleanthous, Structure and function of the *Escherichia coli* Tol-Pal stator protein TolR. *J. Biol. Chem.* **290**, 26675–26687 (2015).
13. K. Kampfenkel, V. Braun, Membrane topologies of the TolQ and TolR proteins of *Escherichia coli*: Inactivation of TolQ by a missense mutation in the proposed first transmembrane segment. *J. Bacteriol.* **175**, 4485–4491 (1993).
14. A. Vianney, T. M. Lewin, W. F. Beyer Jr., J. C. Lazzaroni, R. Portalier, R. E. Webster, Membrane topology and mutational analysis of the TolQ protein of *Escherichia coli* required for the uptake of macromolecules and cell envelope integrity. *J. Bacteriol.* **176**, 822–829 (1994).
15. V. Braun, C. Herrmann, Point mutations in transmembrane helices 2 and 3 of ExbB and TolQ affect their activities in *Escherichia coli* K-12. *J. Bacteriol.* **186**, 4402–4406 (2004).
16. J. C. Lazzaroni, P. Germon, M. C. Ray, A. Vianney, The Tol proteins of *Escherichia coli* and their involvement in the uptake of biomolecules and outer membrane stability. *FEMS Microbiol. Lett.* **177**, 191–197 (1999).
17. X. Y. Zhang, E. L. Goemaere, R. Thomé, M. Gavioli, E. Cascales, R. Lloubès, Mapping the interactions between *Escherichia coli* tol subunits: Rotation of the TolR transmembrane helix. *J. Biol. Chem.* **284**, 4275–4282 (2009).
18. X. Y. Zhang, E. L. Goemaere, N. Seddiki, H. Célia, M. Gavioli, E. Cascales, R. Lloubes, Mapping the interactions between *Escherichia coli* TolQ transmembrane segments. *J. Biol. Chem.* **286**, 11756–11764 (2011).
19. J. C. Lazzaroni, A. Vianney, J. L. Popot, H. Bénédetti, F. Samatey, C. Lazdunski, R. Portalier, V. Géli, Transmembrane alpha-helix interactions are required for the functional assembly of the *Escherichia coli* Tol complex. *J. Mol. Biol.* **246**, 1–7 (1995).
20. P. Germon, T. Clavel, A. Vianney, R. Portalier, J. C. Lazzaroni, Mutational analysis of the *Escherichia coli* K-12 TolA N-terminal region and characterization of its TolQ-interacting domain by genetic suppression. *J. Bacteriol.* **180**, 6433–6439 (1998).
21. L. Journet, A. Rigal, C. Lazdunski, H. Bénédetti, Role of TolR N-terminal, central, and C-terminal domains in dimerization and interaction with TolA and tolQ. *J. Bacteriol.* **181**, 4476–4484 (1999).

22. R. Masilamani, M. B. Cian, Z. D. Dalebroux, *Salmonella* Tol-Pal reduces outer membrane glycerophospholipid levels for envelope homeostasis and survival during bacteremia. *Infect. Immun.* **86**, e00173-18 (2018).
23. E. L. Goemaere, E. Cascales, R. Lloubès, Mutational analyses define helix organization and key residues of a bacterial membrane energy-transducing complex. *J. Mol. Biol.* **366**, 1424–1436 (2007).
24. J. F. Dubuisson, A. Vianney, N. Hugouvieux-Cotte-Pattat, J. C. Lazzaroni, Tol-Pal proteins are critical cell envelope components of *Erwinia chrysanthemi* affecting cell morphology and virulence. *Microbiology (Reading)* **151**, 3337–3347 (2005).
25. J. A. Gaspar, J. A. Thomas, C. L. Marolda, M. A. Valvano, Surface expression of O-specific lipopolysaccharide in *Escherichia coli* requires the function of the TolA protein. *Mol. Microbiol.* **38**, 262–275 (2000).
26. H. Hirakawa, K. Suzue, K. Kurabayashi, H. Tomita, The Tol-Pal system of uropathogenic *Escherichia coli* is responsible for optimal internalization into and aggregation within bladder epithelial cells, colonization of the urinary tract of mice, and bacterial motility. *Front. Microbiol.* **10**, 1827 (2019).
27. H. Abdelhamed, J. Lu, M. L. Lawrence, A. Karsi, Involvement of *tolQ* and *tolR* genes in *Edwardsiella ictaluri* virulence. *Microb. Pathog.* **100**, 90–94 (2016).
28. Q. Li, Z. Li, X. Fei, Y. C. Tian, G. D. Zhou, Y. H. Hu, S. F. Wang, H. Y. Shi, The role of TolA, TolB, and TolR in cell morphology, OMVs production, and virulence of *Salmonella* choleraesuis. *AMB Express* **12**, 5 (2022).
29. M. Witty, C. Sanz, A. Shah, J. G. Grossmann, K. Mizuguchi, R. N. Perham, B. Luisi, Structure of the periplasmic domain of *Pseudomonas aeruginosa* TolA: Evidence for an evolutionary relationship with the TonB transporter protein. *EMBO J.* **21**, 4207–4218 (2002).
30. C. Deprez, R. Lloubès, M. Gavioli, D. Marion, F. Guerlesquin, L. Blanchard, Solution structure of the *E.coli* TolA C-terminal domain reveals conformational changes upon binding to the phage g3p N-terminal domain. *J. Mol. Biol.* **346**, 1047–1057 (2005).
31. C. G. Ford, S. Kolappan, H. T. Phan, M. K. Waldor, H. C. Winther-Larsen, L. Craig, Crystal structures of a CTXφ pIII domain unbound and in complex with a *Vibrio cholerae* TolA domain reveal novel interaction interfaces. *J. Biol. Chem.* **287**, 36258–36272 (2012).
32. C. Li, Y. Zhang, M. Vankemmelbeke, O. Hecht, F. S. Aleanizy, C. Macdonald, G. R. Moore, R. James, C. N. Penfold, Structural evidence that colicin A protein binds to a novel binding site of TolA protein in *Escherichia coli* periplasm. *J. Biol. Chem.* **287**, 19048–19057 (2012).
33. L. M. Parsons, A. Grishaev, A. Bax, The periplasmic domain of TolR from *Haemophilus influenzae* forms a dimer with a large hydrophobic groove: NMR solution structure and comparison to SAXS data. *Biochemistry* **47**, 3131–3142 (2008).
34. D. P. Williams-Jones, M. N. Webby, C. E. Press, J. M. Gradon, S. R. Armstrong, J. Szczepaniak, C. Kleanthous, Tunable force transduction through the *Escherichia coli* cell envelope. *Proc. Natl. Acad. Sci. U.S.A.* **120**, e2306707120 (2023).
35. S. Kojima, D. F. Blair, Conformational change in the stator of the bacterial flagellar motor. *Biochemistry* **40**, 13041–13050 (2001).
36. H. Celia, N. Noinaj, S. D. Zakharov, E. Bordignon, I. Botos, M. Santamaria, T. J. Barnard, W. A. Cramer, R. Lloubes, S. K. Buchanan, Structural insight into the role of the Ton complex in energy transduction. *Nature* **538**, 60–65 (2016).
37. H. Celia, I. Botos, X. Ni, T. Fox, N. De Val, R. Lloubes, J. Jiang, S. K. Buchanan, Cryo-EM structure of the bacterial Ton motor subcomplex ExbB-ExbD provides information on structure and stoichiometry. *Commun. Biol.* **2**, 358 (2019).
38. M. Santiveri, A. Roa-Eguiara, C. Kühne, N. Wadhwa, H. Hu, H. C. Berg, M. Erhardt, N. M. I. Taylor, Structure and function of stator units of the bacterial flagellar motor. *Cell* **183**, 244–257.e16 (2020).
39. J. C. Deme, S. Johnson, O. Vickery, A. Aron, H. Monkhouse, T. Griffiths, R. H. James, B. C. Berks, J. W. Coulton, P. J. Stansfeld, S. M. Lea, Structures of the stator complex that drives rotation of the bacterial flagellum. *Nat. Microbiol.* **5**, 1553–1564 (2020).
40. Y. W. Lai, P. Ridone, G. Peralta, M. M. Tanaka, M. A. B. Baker, Evolution of the stator elements of rotary prokaryote motors. *J. Bacteriol.* **202**, e00557–19 (2020).
41. M. F. El-Badawy, F. I. Abou-Elazm, M. S. Omar, M. E. El-Naggar, I. A. Maghrabi, The first saudi study investigating the plasmid-borne aminoglycoside and sulfonamide resistance among *Acinetobacter baumannii* clinical isolates genotyped by RAPD-PCR: The declaration of a novel allelic variant called *aac(6′)-SL* and three novel mutations in the *sul1* gene in the acinetobacter plasmid(s). *Infect Drug Resist.* **14**, 4739–4756 (2021).
42. C. L. Williams, H. M. Neu, Y. A. Alamneh, R. M. Reddinger, A. C. Jacobs, S. Singh, R. Abu-Taleb, S. L. J. Michel, D. V. Zurawski, D. S. Merrell, Characterization of *Acinetobacter baumannii* copper resistance reveals a role in virulence. *Front. Microbiol.* **11**, 16 (2020).
43. F. Runci, V. Gentile, E. Frangipani, G. Rampioni, L. Leoni, M. Lucidi, D. Visaggio, G. Harris, W. Chen, J. Stahl, B. Averhoff, P. Visca, Contribution of active iron uptake to *Acinetobacter baumannii* pathogenicity. *Infect. Immun.* **87**, e00755-18 (2019).
44. M. S. Mulani, E. E. Kamble, S. N. Kumkar, M. S. Tawre, K. R. Pardesi, Emerging strategies to combat ESKAPE pathogens in the era of antimicrobial resistance: A review. *Front. Microbiol.* **10**, 539 (2019).
45. M. van Kempen, S. S. Kim, C. Tumescheit, M. Mirdita, J. Lee, C. L. M. Gilchrist, J. Söding, M. Steinegger, Fast and accurate protein structure search with Foldseek. *Nat. Biotechnol.* **42**, 243–246 (2024).
46. T. Nishikino, N. Takekawa, D. P. Tran, J. I. Kishikawa, M. Hirose, S. Onoe, S. Kojima, M. Homma, A. Kitao, T. Kato, K. Imada, Structure of MotA, a flagellar stator protein, from hyperthermophile. *Biochem. Biophys. Res. Commun.* **631**, 78–85 (2022).
47. E. Krissinel, K. Henrick, Inference of macromolecular assemblies from crystalline state. *J. Mol. Biol.* **372**, 774–797 (2007).
48. E. L. Goemaere, A. Devert, R. Lloubès, E. Cascales, Movements of the TolR C-terminal domain depend on TolQR ionizable key residues and regulate activity of the Tol complex. *J. Biol. Chem.* **282**, 17749–17757 (2007).
49. V. Braun, A. C. Ratliff, H. Celia, S. K. Buchanan, Energization of outer membrane transport by the ExbB ExbD molecular motor. *J. Bacteriol.* **205**, e0003523 (2023).
50. S. Rao, G. Klesse, P. J. Stansfeld, S. J. Tucker, M. S. P. Sansom, A heuristic derived from analysis of the ion channel structural proteome permits the rapid identification of hydrophobic gates. *Proc. Natl. Acad. Sci. U.S.A.* **116**, 13989–13995 (2019).
51. A. Punjani, D. J. Fleet, 3D variability analysis: Resolving continuous flexibility and discrete heterogeneity from single particle cryo-EM. *J. Struct. Biol.* **213**, 107702 (2021).
52. E. Cascales, M. Gavioli, J. N. Sturgis, R. Lloubès, Proton motive force drives the interaction of the inner membrane TolA and outer membrane pal proteins in *Escherichia coli*. *Mol. Microbiol.* **38**, 904–915 (2000).
53. J. Jumper, R. Evans, A. Pritzel, T. Green, M. Figurnov, O. Ronneberger, K. Tunyasuvunakool, R. Bates, A. Zidek, A. Potapenko, A. Bridgland, C. Meyer, S. A. A. Kohl, A. J. Ballard, A. Cowie, B. Romera-Paredes, S. Nikolov, R. Jain, J. Adler, D. Hassabis, Highly accurate protein structure prediction with AlphaFold. *Nature* **596**, 583–589 (2021).
54. M. N. Webby, D. P. Williams-Jones, C. Press, C. Kleanthous, Force-generation by the trans-envelope Tol-Pal system. *Front. Microbiol.* **13**, 852176 (2022).
55. P. J. Loll, K. C. Grasty, D. D. Shultis, N. J. Guzman, M. C. Wiener, Discovery and structural characterization of the D-box, a conserved TonB motif that couples an inner-membrane motor to outer-membrane transport. *J. Biol. Chem.* **300**, 105723 (2024).
56. M. Zinke, M. Lejeune, A. Mechaly, B. Bardiaux, I. G. Boneca, P. Delepelaire, N. Izadi-Pruneyre, Ton motor conformational switch and peptidoglycan role in bacterial nutrient uptake. *Nat. Commun.* **15**, 331 (2024).
57. A. C. Ratliff, S. K. Buchanan, H. Celia, The ton motor. *Front. Microbiol.* **13**, 852955 (2022).
58. P. Demchick, A. L. Koch, The permeability of the wall fabric of *Escherichia coli* and *Bacillus subtilis*. *J. Bacteriol.* **178**, 768–773 (1996).
59. M. Rieu, R. Krutyholowa, N. M. I. Taylor, R. M. Berry, A new class of biological ion-driven rotary molecular motors with 5:2 symmetry. *Front. Microbiol.* **13**, 948383 (2022).
60. J. J. Kerrigan, Q. Xie, R. S. Ames, Q. Lu, Production of protein complexes via co-expression. *Protein Expr. Purif.* **75**, 1–14 (2011).
61. A. Olerinyova, A. Sonn-Segev, J. Gault, C. Eichmann, J. Schimpf, A. H. Kopf, L. S. P. Rudden, D. Ashkinadze, R. Bomba, L. Frey, J. Greenwald, M. T. Degiacomi, R. Steinhilper, J. A. Killian, T. Friedrich, R. Riek, W. B. Struwe, P. Kukura, Mass photometry of membrane proteins. *Chem* **7**, 224–236 (2021).
62. A. Punjani, J. L. Rubinstein, D. J. Fleet, M. A. Brubaker, cryoSPARC: Algorithms for rapid unsupervised cryo-EM structure determination. *Nat. Methods* **14**, 290–296 (2017).
63. A. Punjani, H. Zhang, D. J. Fleet, Non-uniform refinement: Adaptive regularization improves single-particle cryo-EM reconstruction. *Nat. Methods* **17**, 1214–1221 (2020).
64. E. F. Pettersen, T. D. Goddard, C. C. Huang, G. S. Couch, D. M. Greenblatt, E. C. Meng, T. E. Ferrin, UCSF Chimera—A visualization system for exploratory research and analysis. *J. Comput. Chem.* **25**, 1605–1612 (2004).
65. P. Emsley, K. Cowtan, Coot: Model-building tools for molecular graphics. *Acta Crystallogr. D Biol. Crystallogr.* **60**, 2126–2132 (2004).
66. E. Krissinel, K. Henrick, Secondary-structure matching (SSM), a new tool for fast protein structure alignment in three dimensions. *Acta Crystallogr. D Biol. Crystallogr.* **60**, 2256–2268 (2004).
67. D. Liebschner, P. V. Afonine, M. L. Baker, G. Bunkóczi, V. B. Chen, T. I. Croll, B. Hintze, L. W. Hung, S. Jain, A. J. McCoy, N. W. Moriarty, R. D. Oeffner, B. K. Poon, M. G. Prisant, R. J. Read, J. S. Richardson, D. C. Richardson, M. D. Sammito, O. V. Sobolev, D. H. Stockwell, T. C. Terwilliger, A. G. Urzhumtsev, L. L. Videau, C. J. Willims, P. D. Adams, Macromolecular structure determination using x-rays, neutrons and electrons: Recent developments in Phenix. *Acta Crystallogr. D. Struct. Biol.* **75**, 861–877 (2019).
68. K. Yamashita, C. M. Palmer, T. Burnley, G. N. Murshudov, Cryo-EM single-particle structure refinement and map calculation using Servalcat. *Acta Crystallogr. D. Struct. Biol.* **77**, 1282–1291 (2021).
69. A. Brown, F. Long, R. A. Nicholls, J. Toots, P. Emsley, G. Murshudov, Tools for macromolecular model building and refinement into electron cryo-microscopy reconstructions. *Acta Crystallogr. D Biol. Crystallogr.* **71**, 136–153 (2015).
70. P. V. Afonine, B. K. Poon, R. J. Read, O. V. Sobolev, T. C. Terwilliger, A. Urzhumtsev, P. D. Adams, Real-space refinement in PHENIX for cryo-EM and crystallography. *Acta Crystallogr. D. Struct. Biol.* **74**, 531–544 (2018).
71. L. L. C. Schrödinger, "The PyMOL Molecular Graphics System, Version 2.3." (2020); http://pymol.org/pymol.

72. P. C. Hsu, F. Samsudin, J. Shearer, S. Khalid, It is complicated: Curvature, diffusion, and lipid sorting within the two membranes of *Escherichia coli*. *J. Phys. Chem. Lett.* **8**, 5513–5518 (2017).
73. E. L. Wu, P. J. Fleming, M. S. Yeom, G. Widmalm, J. B. Klauda, K. G. Fleming, W. Im, *E. coli* outer membrane and interactions with OmpLA. *Biophys. J.* **106**, 2493–2502 (2014).
74. V. W. Rowlett, V. Mallampalli, A. Karlstaedt, W. Dowhan, H. Taegtmeyer, W. Margolin, H. Vitrac, Impact of membrane phospholipid alterations in *Escherichia coli* on cellular function and bacterial stress adaptation. *J. Bacteriol.* **199**, e00849-16 (2017).
75. S. Jo, J. B. Lim, J. B. Klauda, W. Im, CHARMM-GUI Membrane Builder for mixed bilayers and its application to yeast membranes. *Biophys. J.* **97**, 50–58 (2009).
76. E. L. Wu, X. Cheng, S. Jo, H. Rui, K. C. Song, E. M. Dávila-Contreras, Y. Qi, J. Lee, V. Monje-Galvan, R. M. Venable, J. B. Klauda, W. Im, CHARMM-GUI Membrane Builder toward realistic biological membrane simulations. *J. Comput. Chem.* **35**, 1997–2004 (2014).
77. S. Jo, T. Kim, W. Im, Automated builder and database of protein/membrane complexes for molecular dynamics simulations. *PLOS ONE* **2**, e880 (2007).
78. J. C. Phillips, D. J. Hardy, J. D. C. Maia, J. E. Stone, J. V. Ribeiro, R. C. Bernardi, R. Buch, G. Fiorin, J. Hénin, W. Jiang, R. McGreevy, M. C. R. Melo, B. K. Radak, R. D. Skeel, A. Singharoy, Y. Wang, B. Roux, A. Aksimentiev, Z. Luthey-Schulten, E. Tajkhorshid, Scalable molecular dynamics on CPU and GPU architectures with NAMD. *J. Chem. Phys.* **153**, 044130 (2020).
79. J. Huang, S. Rauscher, G. Nawrocki, T. Ran, M. Feig, B. L. de Groot, H. Grubmüller, A. D. MacKerell Jr., CHARMM36m: An improved force field for folded and intrinsically disordered proteins. *Nat. Methods* **14**, 71–73 (2017).
80. J. B. Klauda, R. M. Venable, J. A. Freites, J. W. O'Connor, D. J. Tobias, C. Mondragon-Ramirez, I. Vorobyov, A. D. MacKerell Jr., R. W. Pastor, Update of the CHARMM all-atom additive force field for lipids: Validation on six lipid types. *J. Phys. Chem. B* **114**, 7830–7843 (2010).
81. U. Essmann, L. Perera, M. L. Berkowitz, T. Darden, H. Lee, L. G. Pedersen, A smooth particle mesh Ewald method. *J. Chem. Phys.* **103**, 8577–8593 (1995).
82. W. Humphrey, A. Dalke, K. Schulten, VMD: Visual molecular dynamics. *J. Mol. Graph.* **14**, 33–38 (1996).
83. N. Michaud-Agrawal, E. J. Denning, T. B. Woolf, O. Beckstein, MDAnalysis: A toolkit for the analysis of molecular dynamics simulations. *J. Comput. Chem.* **32**, 2319–2327 (2011).
84. O. S. Smart, J. G. Neduvelil, X. Wang, B. A. Wallace, M. S. Sansom, HOLE: A program for the analysis of the pore dimensions of ion channel structural models. *J. Mol. Graph.* **14**, 354–360 (1996).
85. L. G. Trabuco, E. Villa, E. Schreiner, C. B. Harrison, K. Schulten, Molecular dynamics flexible fitting: A practical guide to combine cryo-electron microscopy and X-ray crystallography. *Methods* **49**, 174–180 (2009).
86. M. Mirdita, K. Schütze, Y. Moriwaki, L. Heo, S. Ovchinnikov, M. Steinegger, ColabFold: Making protein folding accessible to all. *Nat. Methods* **19**, 679–682 (2022).
87. E. C. Meng, T. D. Goddard, E. F. Pettersen, G. S. Couch, Z. J. Pearson, J. H. Morris, T. E. Ferrin, UCSF ChimeraX, tools for structure building and analysis. *Protein Sci.* **32**, e4792 (2023).
88. J. D. Hunter, Matplotlib: A 2D graphics environment. *Comput. Sci. Eng.* **9**, 90–95 (2007).
89. R. A. Laskowski, J. Jabłońska, L. Pravda, R. S. Vařeková, J. M. Thornton, PDBsum: Structural summaries of PDB entries. *Protein Sci.* **27**, 129–134 (2018).
90. X. Robert, P. Gouet, Deciphering key features in protein structures with the new ENDscript server. *Nucleic Acids Res.* **42**, W320–W324 (2014).
91. J. R. Jungck, M. Cebeci, Wenxiang 3.0: Evolutionary visualization of α, π, and 3/10 helices. *Evol. Bioinform Online* **18**, 11769343221101014 (2022).

Acknowledgments: We thank our colleagues C. Samper (UofC) for valuable suggestions in cloning *Ac*TolQ-TolR construct, N. Watanabe (UofC), and P. Stogios (UofT) for discussion of protein purification. **Funding:** This work was supported by the National Institutes of Health/National Institutes of Health contract #75N93022C00035 (A.S. and D.B.), National Institutes of Health/National Institutes of Health contract HHSN272201700060C (Z.O.), National Institutes of Health/National Institute of General Medical Sciences grant R35 GM145365 (Z.O.), Department of Energy DE-SC0019600 (Y.G.), Canadian Institutes of Health Research PJT-180245 (D.P.T.), Canada Research Chairs (D.P.T.), and Digital Research Alliance of Canada (D.P.T.). Some results in this report were supported by the use of a mass photometer that was supported by the award S10OD030312-01 from the National Institutes of Health. We thank the Cryo-Electron Microscopy Facility (CEMF) at UT Southwestern Medical Center, which has been supported by grants RP170644 and RP220582 from the Cancer Prevention and Research Institute of Texas (CPRIT), for maintaining a Titan Krios microscope. **Author contributions:** Conceptualization: E.K., Y.G., H.M.K., D.P.T., D.B., Z.O., and A.S. conceived the project. Methodology: A.S., E.K., Y.G., H.M.K., R.D.L., B.Q., and T.E. designed the experiments. Investigation: R.D.L. cloned *Ac*TolQ construct; E.K. cloned *Ac*TolQ-TolR constructs; E.K. performed expression and purification of all constructs; E.K. performed screening to stabilize all purified membrane proteins and mass photometry assays; T.E. performed mass photometry assays and grids preparation; B.Q. and Y.G. performed single-particle reconstruction; Y.G., D.B., and Z.O. validated models and maps; Y.G. performed 3D visualization assay; H.M.K. performed MD simulations; E.K. performed structure guided analysis and AlphaFold modeling; E.K., D.B., and Z.O. worked on mechanistic models. Supervision: A.S., D.B., Z.O., and D.P.T. Writing—original draft: E.K. Writing—review and editing: E.K., Y.G., H.M.K., Z.O., D.P.T., D.B., and A.S. **Competing interests:** Y.G., Z.O., and D.B. are cofounders of Ligo Analytics. Y.G. serves as the CEO of Ligo Analytics and is currently employed by Ligo Analytics. Z.O. is a cofounder of HKL Research, a company that develops and distributes software for x-ray crystallography. The authors declare that they have no other competing interests. **Data and materials availability:** The atomic coordinates of apo *Ac*TolQ structure (PDB: 9AVI) and maps (EMD-43902) have been deposited in the Protein Data Bank (http://wwpdb.org/) and the Electron Microscopy Data Bank (https://ebi.ac.uk/emdb/), respectively. The *Ac*TolQ-TolR structure (PDB: 8VLW) and maps (EMD-43346) can be found in the mentioned above databases as well. All other data needed to evaluate the conclusions in this paper are present in the paper and/or the Supplementary Materials.

Submitted 10 June 2024
Accepted 28 February 2025
Published 4 April 2025
10.1126/sciadv.adq9845